Julius-Maximilians-Universität-Würzburg

Bachelor Thesis

Search for Positronium Recombination Lines with the Effelsberg 100m Telescope

Supervisors:
Prof. Dr. Matthias Kadler
Prof. Dr. Ingo Scholtes

Academic Advisors:
Jonas Heßdörfer
Florian Eppel
Dr. Thomas Siegert

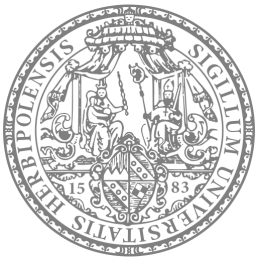

A thesis submitted in fulfillment of the requirements for the degree of Bachelor of Science

in the group of

Prof. Dr. Matthias Kadler
Chair of Astronomy

Author:
Lovis Haury

December 2024

Zusammenfassung

Diese Arbeit stellt eine Methode zur Suche nach Rekombinationslinien im Radiobereich des elektromagnetischen Spektrums vor, die durch die Kombination mehrerer Einzelmessungen eine signifikante Erhöhung der Empfindlichkeit ermöglicht. Die Detektion von Rekombinationslinien im Radiobereich, insbesondere Rekombinationslinien von Positronium, ist ein wesentlicher Aspekt in der Suche nach Dunkler Materie, da die Stärke der Linie Aufschluss über die Menge an Positronium an den beobachteten Orten gibt. Dies ist entscheidend für die Berechnung des Annihilationsquerschnitts und für Erkenntnisse zur möglichen Selbst-Annihilation von Dunkler Materie.
Die in dieser Arbeit vorgestellte Methode wird auf den Frequenzbereich von $13-15\,\mathrm{GHz}$ angewendet und nutzt Daten, die zwischen den Jahren 2021 und 2024 mit dem 100 m Radioteleskop in Effelsberg im Rahmen des TELAMON-Projekts gesammelt wurden. Die Funktionsweise dieses Ansatzes wird demonstriert und es werden Wasserstoff-Rekombinationslinien (H76α – H79α) in den Kalibratorquellen NGC7027 und W3OH detektiert. Für die Amplituden und den Fluss der Rekombinationslinien von Positronium (Ps60α – Ps62α) werden obere Grenzen berechnet. Für die überlagerten Daten des gesamten Beobachtungszeitraums ergibt sich eine 3σ-Obergrenze mit einer Flussdichte von $0.6-0.7\,\mathrm{mJy}$, je nach Rekombinationslinie.
Zusätzlich werden für die Kalibratorquelle NGC7027 zwei Methoden verglichen. Die "Single"-Methode, die die obere Grenze für jede Rekombinationslinie von NGC7027 einzeln bestimmt, liefert eine 3σ-Obergrenze von $5.1-7.2\,\mathrm{mJy}$. Im Gegensatz dazu ergibt die "Combined"-Methode, die die drei Linien miteinander verknüpft und dann die obere Grenze bestimmt, eine 3σ-Obergrenze von $3.6-4.0\,\mathrm{mJy}$.

Abstract

This thesis introduces a method for detecting recombination lines in the radio regime of the electromagnetic spectrum, significantly enhancing sensitivity by combining multiple measurements. The detection of recombination lines in the radio range, especially recombination lines of positronium, is a key aspect in the search for dark matter, as the strength of the line provides insight into the amount of positronium at the observed locations. This is crucial for calculating the annihilation cross-section and gaining insights to potential self-annihilation of dark matter. The method presented in this thesis is applied to the frequency range of $13-15\,\mathrm{GHz}$ and uses data collected between the years $2021-2024$ with the 100 m radio telescope in Effelsberg as part of the TELAMON project. The functionality of this approach is demonstrated and hydrogen recombination lines are detected (H76α – H79α) in the calibrator sources NGC7027 and W3OH. For recombination lines of positronium (Ps60α – Ps62α), upper limits are calculated. For the combined data over the entire observation period, this results in a 3σ upper limit with a flux density of $0.6-0.7\,\mathrm{mJy}$, depending on the spectral line.
Additionally, two methods are compared using data of the calibrator source NGC7027 only. The "single" method, which determines the upper limit for each recombination line of NGC7027 individually, yields a 3σ upper limit of $5.1-7.2\,\mathrm{mJy}$. In contrast, the "combined" method, which links the three expected lines and then determines the upper limit, results in a 3σ upper limit of $3.6-4.0\,\mathrm{mJy}$.

Contents

1 | Introduction

Findings from the fields of cosmology and astrophysics provide compelling support for the hypothesis that dark matter exists (Komatsu et al., 2009, Bertone et al., 2005). Despite many studies of galaxies and the cosmic background radiation (CMB) showing that dark matter accounts for about 26% of the cosmic mass-energy density and 84% of the density of normal matter in the universe today (Staveley-Smith et al., 2022), little is known about its fundamental properties. To better understand the formation and evolution of galaxies, it is important to understand the distribution of dark matter as well as its interaction with normal matter.

The search for dark matter signals covers the entire electromagnetic spectrum, from long-wave radio signals to high-energy gamma radiation (Staveley-Smith et al., 2022, Siegert, 2023). The data used in this thesis is exclusively located in the low-frequency range. This low-frequency range, the radio regime, is mostly sensitive to synchrotron radiation emitted by charged particles (e.g. protons, electrons, or their antiparticles) gyrating in existing magnetic fields (Borriello et al., 2009). The potential for dark matter particles to self-annihilate suggests that they could produce high-energy electrons, positrons, photons, and neutrinos (Jung et al., 2022). The self-annihilation rate depends on the velocity-averaged annihilation cross-section and the mass of the dark matter particle (Bhattacharjee, 2022). Studies of globular clusters (Staveley-Smith et al., 2022) have revealed significant limits on the annihilation cross-section of dark matter particles from measurements of positronium recombination lines. Positronium, a bound state of an electron and a positron, is expected to form from the byproducts of dark matter annihilation and could be detected in the radio band (Staveley-Smith et al., 2022). Future radio observations, including those with the Square Kilometer Array, are expected to further refine these limits (Storm et al., 2017).

In this context, my research focuses on the 13 – 15 GHz radio band, with the aim of detecting positronium annihilation lines by combining several hundred of hours of radio data from the Effelsberg 100 m radio telescope. In this 2 GHz wide band, three positronium-alpha lines are expected: Ps60α at a frequency of 14.85827 GHz, Ps61α at 14.14514 GHz, and Ps62α at 13.47692 GHz. By stacking radio data collected between 2021 and 2024 with the Effelsberg 100m radio telescope within the TELAMON[1] program, the sensitivity increases, allowing for the derivation of low upper limits on the spectral line flux density. This thesis therefore contributes to the broader search for potential dark matter signatures.

[1] https://telamon.astro.uni-wuerzburg.de/

2 | Theoretical Background

2.1 Electromagnetic Spectrum

Electromagnetic radiation describes the transmission of energy in the form of electromagnetic waves or photons. This exchange of energy plays a central role for us here on Earth, but also in space, since almost all processes in the universe generate radiation in different wavelength ranges through the interaction of matter and energy (NASA, 2010). The electromagnetic spectrum ranges from low-frequency radio radiation with energies less than 10^{-14} eV to ultra-high-energy gamma radiation in the TeV range. However, a significant portion of this radiation is absorbed or scattered by Earth's magnetic field and atmosphere, meaning that only a limited range of the electromagnetic spectrum can be observed on Earth (Rees, 2001). Figure 2.1 shows the frequency ranges of atmospheric opacity. This includes visible light and in particular radio waves with wavelengths of around 10 cm to 10 m which will play a significant role for the observations later in this thesis.

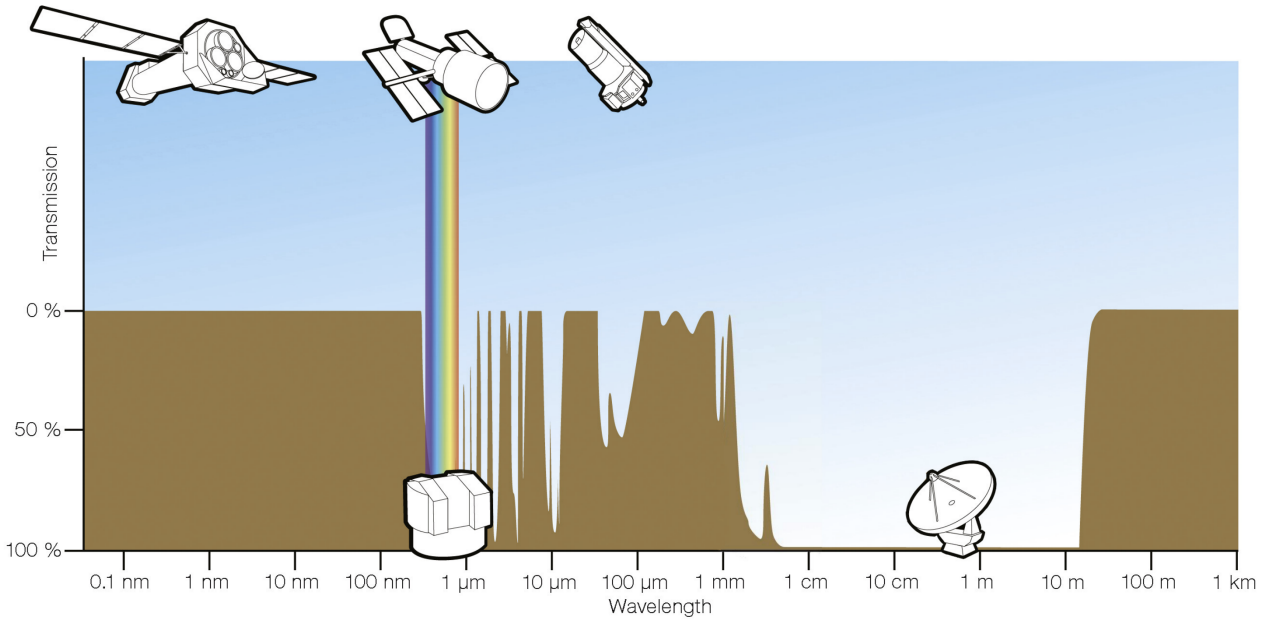

Figure 2.1: The brown area shows the level of transmission of electromagnetic radiation in Earth's atmosphere. Two windows can be seen in which the atmosphere is mostly transmissive. One is the range of visible light, marked by the rainbow, the other is in the radio range, marked by the radio telescope. Credit: https://www.eso.org/public/images/atm_opacity/

2.2 TELAMON

The data used in this project were all recorded as part of the TELAMON project (Eppel et al., 2024). Over the course of the project, more than 100 different radio sources[1] have been observed at regular intervals using the 100 m radio telescope in Effelsberg, Germany. This telescope is operated by the Max Planck Institute for Radio Astronomy (MPIfR) in Bonn. With the exception of calibrator sources, which are partially located within our galaxy, all observed sources are active galactic nuclei (AGN). Figure 2.2 provides an overview of the location of all sources used in this thesis. More details concerning the observation with the Effelsberg 100 m radio telescope is given in Sec. 3.1.

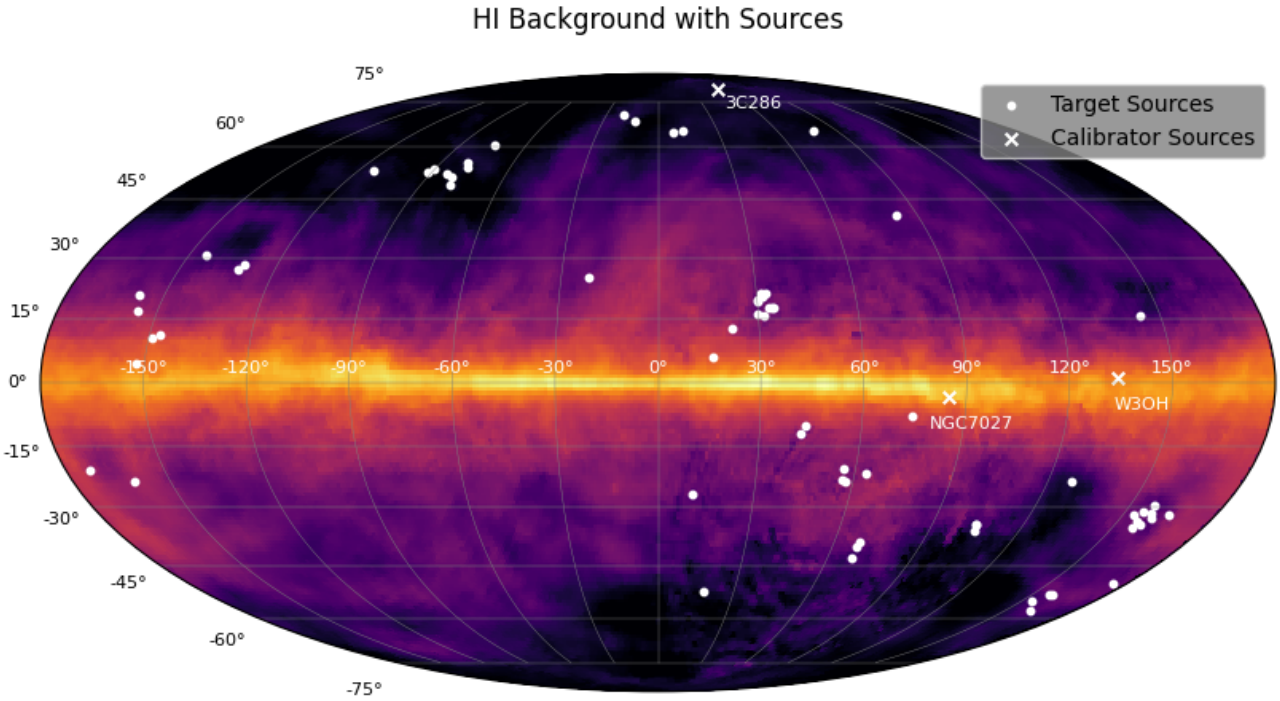

Figure 2.2: Locations of observed sources in galactic coordinates plotted on top of the HI 21 cm map of neutral hydrogen. The dots represent the target sources used for this thesis, the crosses represent the three calibrator sources. Credit: (background) Bekhti et al. (2016)

2.3 Active Galactic Nuclei

The following information is taken from Beckmann & Shrader (2012), Rosswog & Brüggen (2007), Urry & Padovani (1995), Antonucci (1993) and Mannheim & Siegert (2024). AGN are among the most powerful non-explosive objects in the universe. Their energy is primarily generated through the accretion of matter onto a supermassive black hole (SMBH).
The AGN is described as the core of active galaxies, including not only the SMBH but also surrounding structures, such as the accretion disk and the dust torus. Unlike normal galaxies, active galaxies emit radiation across the entire electromagnetic spectrum, rather than peaking in the optical range. This results in luminosities of L $\sim 10^{10}$ $L_\odot$ that are so bright that they can exceed the luminosity of the entire rest of the galaxy. This also means that the emission can not be based on nuclear fusion as it is in stars, but has to come from a non-thermal process, from the accretion of mass of the SMBH.

[1] https://telamon.astro.uni-wuerzburg.de/sources

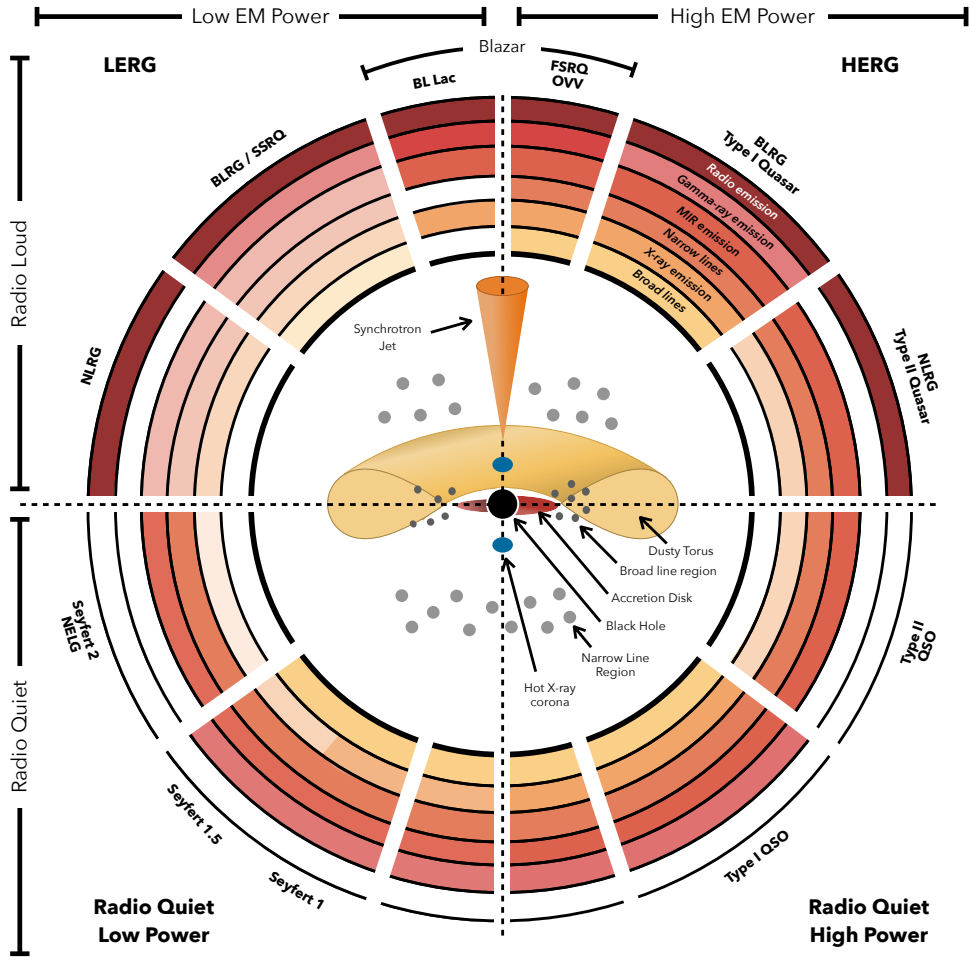

Figure 2.3: The supermassive black hole (SMBH) forms the core of the AGN structure shown. Surrounding it, key features such as the accretion disk, electron plasma, broad and narrow line regions, dust torus, and relativistic jets can be seen. Encircling the central schematic, various nomenclatures corresponding to distinct viewing angles and observational characteristics are illustrated. Credit: Thorne et al. (2022).

AGN can be categorized into certain groups, mainly depending on the viewing angle, the power of the central engine and the emitted radio radiation.
Figure 2.3 shows the structure of an AGN, highlighting its various components: SMBH, accretion disk, broad line region, narrow line region, and dust torus. The SMBH forms the center of the AGN and is surrounded by the accretion disk. The material in the accretion disk, consisting of hot gas and dust, heats up due to friction as it spirals inward towards the SMBH due to the intense gravitational forces. Just beyond the accretion disk lies the broad line region (BLR), where rapidly moving gas clouds produce emission lines that are broadened due to their high velocities near the supermassive black hole.
Further from the center is the narrow line region (NLR), which contains ionized gas clouds moving at slower speeds, resulting in emission lines that are much narrower compared to those of the BLR. Depending on the amount of radio radiation emitted by the AGN, it can be classified as radio-loud or radio-quiet. Radio-loud AGN are characterized by the presence of prominent relativistic jets, which are powerful, collimated outflows of matter and energy emitted along the axis of the black hole's rotation. The jets play a crucial role in the emitted radio radiation, as the acceleration of particles within them generates synchrotron radiation, which can be observed in the radio regime. The radio-loudness of AGN can be quantified as the ratio between the optical flux F_O and the radio flux F_R (Kellermann et al., 1989):

$$R_L = \frac{F_O}{F_R} \tag{2.1}$$

Sources with $R_L > 10$ are classified as radio-loud, while sources with $R_L \leq 1$ are designated as radio-quiet.

In this thesis, blazars, a subclass of radio-loud AGN, play an important role. They are characterised by the fact that their jet is observed at a small viewing angle, i.e. pointed directly towards Earth. Blazars appear as bright point sources due to relativistic beaming, meaning that intensity increases in the direction of motion due to the relativistic Doppler effect. This subclass is further divided into BL Lac objects and flat spectrum radio quasars (FSRQs), with the difference that BL Lacs have no or only weak optical emission lines.

Most of the radio emission from a blazar is generated by synchrotron radiation, which is produced by highly relativistic particles gyrating in existing magnetic fields. Blazars typically exhibit a double-humped spectral energy distribution (SED), with two characteristic peaks shown in Fig. 2.4. The low-frequency peak corresponds to the synchrotron emission, while the high-frequency peak is usually attributed to inverse Compton scattering in leptonic models (Fossati et al., 1998).

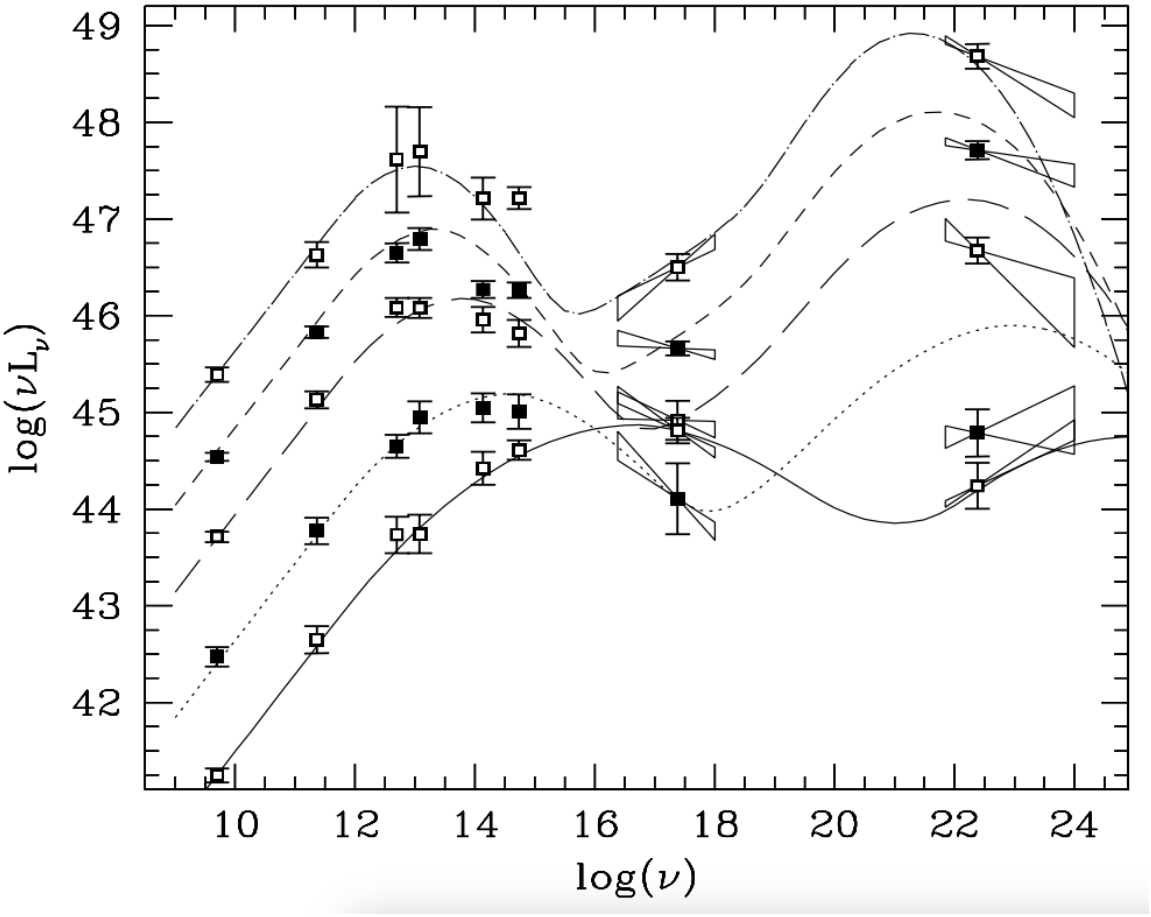

Figure 2.4: The average spectral energy distributions (SEDs) for the "total blazar sample" have been binned according to radio luminosity, irrespective of the original classification. The overlaid curves represent analytic approximations obtained in accordance with the one-parameter family definition in explained in Fossati et al. (1998). Credit: Fossati et al. (1998)

In the case of non-thermal synchrotron radiation, the distribution of electrons $n(\gamma)$ follows a power law (Rybicki & Lightman, 1979):

$$n(\gamma)d\gamma = n_0\gamma^{-p}d\gamma \tag{2.2}$$

$n(\gamma)d\gamma$ describes the number of electrons per unit volume where $\gamma = (1 - v^2/c^2)^{-\frac{1}{2}}$ is the Lorentz factor with c the speed of light in vacuum, v the speed of the accelerated particle and p is referred to as the particle distribution index. This leads to a synchrotron spectrum described by the following power-law distribution:

$$P(\nu) \propto \nu^{-\frac{p-1}{2}} = \nu^{-\alpha}, \tag{2.3}$$

with α being the spectral index. Blazars are also categorized according to the frequency at which their primary emission peak occurs. High peaked BL Lacs (HBL) have a frequency peak above $\nu \geq 10^{15}$ Hz, while low peaked BL Lacs (LBL) have a frequency peak below $\nu < 10^{14}$ Hz. Sources between HBL and LBL are referred to as intermediate peaked BL Lacs (IBL).

2.4 Spectroscopy and Spectral Lines

In astronomy, spectroscopy is an important method for investigating the universe. Spectrographs allow scientists to analyze electromagnetic radiation, making it possible to study the chemical composition, movements, and physical properties of distant objects like stars, nebulae, and galaxies. The properties of the radiation, such as wavelength and intensity, are measured and used to draw conclusions about the physical conditions and elements present (Appenzeller, 2012) The most well-known application demonstrating this is the prism. It breaks down the incident light into individual colors, as the different wavelengths are refracted to different degrees by the glass. This is particularly relevant when looking for deviations at certain frequencies in the spectrum. Spectral lines are frequencies in the spectrum of an atom or molecule that have a higher amplitude compared to other frequencies. They can be produced by various processes, such as electronic transitions between energy states, hyperfine structure transitions, or during annihilation events (Condon & Ransom, 2016).

2.4.1 Electron Transitions Between Energy Levels

Electrons in atoms can take different energy levels. This means that they can absorb energy in the form of photons but can also emit energy. When an atom is in an excited state, it has already absorbed energy. To reach a lower energy state, the atom can emit energy in the form of a photon until it reaches the ground state. The energy of the emitted photon corresponds exactly to the difference in energy levels between the excited state and the lower state. Niels Bohr established a postulate that states that the amount of energy E released in the form of a photon when an electron transitions from orbit n to orbit n' can be described by the formula (Bohr, 1913)

$$E_n - E_{n'} = \hbar\omega. \tag{2.4}$$

Here $\hbar$ is the reduced Planck constant and $\omega = 2\pi\nu$ corresponds to the angular frequency. This relationship is illustrated in Figure 2.5.

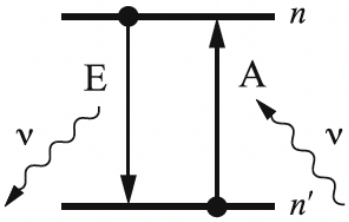

Figure 2.5: Energy transition of an electron from a higher energy level n to a lower level n' and vice versa. During the transition, a photon with frequency ν is emitted or absorbed, accordingly. Credit: Leisi (2006)

These energy states are quantized, which means they cannot be chosen arbitrarily. Therefore, an emitted photon can only assume specific energy values, which in turn leads to discrete frequencies in the spectral range. Following Leisi (2006), these frequencies can be calculated using fundamental principles. Since the electron experiences the Coulomb force F_c, Newtons equations of motion in the radial direction provide the following relationship

$$\frac{mv^2}{r} = F_c = \frac{e^2}{4\pi\epsilon_0 r^2}. \tag{2.5}$$

Here, e is considered as the elementary charge of an electron, m is the reduced mass, v the velocity, r the distance of the two particles and ϵ_0 the vacuum permittivity. Using the angular momentum $L = mvr$, multiplying both sides with mr^3 and solving for r leads to

$$r = \frac{4\pi\epsilon_0}{me^2} L^2. \tag{2.6}$$

To retrieve the frequency of the photon, Eq. (2.5) can be multiplied by r to gain the inner (i.e. potential) energy U of the atom

$$\frac{e^2}{4\pi\epsilon_0 r} = mv^2 = -U. \tag{2.7}$$

The total energy can then be computed as the sum of the kinetic energy E_{kin} and the potential energy E_{pot}:

$$E_{total} = E_{kin} + E_{pot} = \frac{m}{2}v^2 + U = -\frac{m}{2}v^2. \tag{2.8}$$

If the angular momentum $L = mvr$ is used, Eq. (2.8) using Eq. 2.6 results in

$$E_{total} = -\frac{L^2}{2mr^2} = -\frac{m}{2}\frac{e^4}{(4\pi\epsilon_0)^2}\frac{1}{L^2}. \tag{2.9}$$

The angular momentum can be quantized via $L = n\hbar$, which leads to the following formula

$$E_{total} = E_n = -\frac{m}{2}\frac{e^4}{(4\pi\epsilon_0)^2\hbar^2}\frac{1}{n^2} = -R_\infty \frac{1}{n^2}. \tag{2.10}$$

R_∞ describes the Rydberg energy. For hydrogen this energy equals

$$R_\infty = \frac{1}{2}mc^2\alpha^2 = 13.61eV \quad \text{with} \quad \alpha = \frac{e^2}{4\pi\epsilon_0\hbar c}. \tag{2.11}$$

Using Bohrs postulate (Eq. (2.4)), the frequency of the emitted photon can be calculated via

$$\nu_{nn'} = \frac{R_\infty}{2\pi\hbar}\left(\frac{1}{n'^2} - \frac{1}{n^2}\right). \tag{2.12}$$

Depending on the energy level reached after the energy release, the set of possible recombination lines is named differently. Well-known series include the Lyman series, the Balmer series, and the Paschen series, corresponding to electrons falling to the first, second, and third energy levels, respectively. Figure 2.6 illustrates the first series.

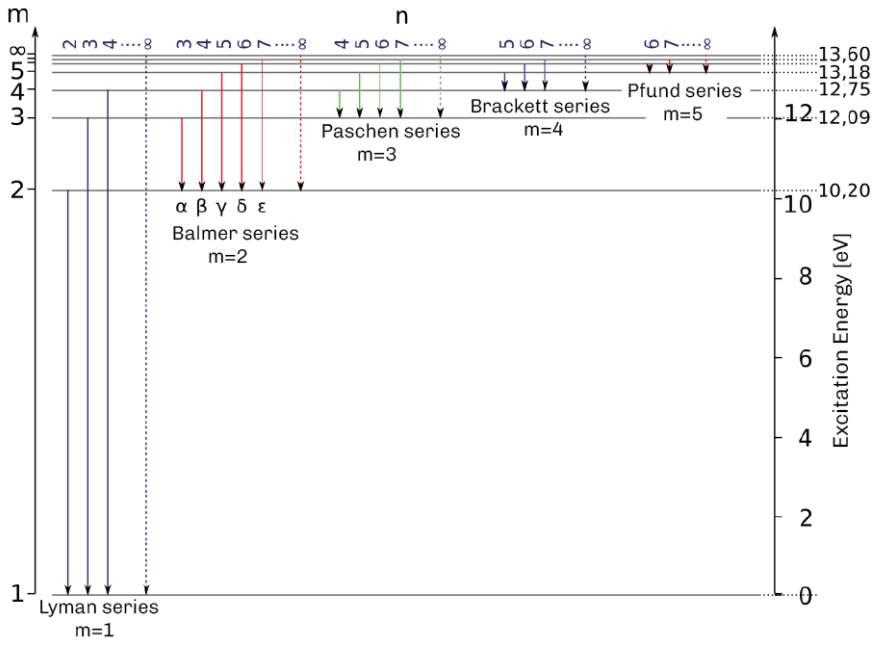

Figure 2.6: Energy levels for the first series of the hydrogen atom, Credit: Scholz (2018)

2.5 Positronium

Positronium is a bound state consisting of an electron (e^-) and its antiparticle, the positron (e^+). The positron has the same mass as the electron but a positive charge. Therefore, positronium is a neutrally charged system with properties similar to a hydrogen atom. The key difference is that positronium does not have an atomic nucleus but only two oppositely charged particles bound by the Coulomb force (Cassidy & Mills Jr, 2007).

The structure of positronium compared to hydrogen, based on Bohr's atomic model, is shown in Fig. 2.7.

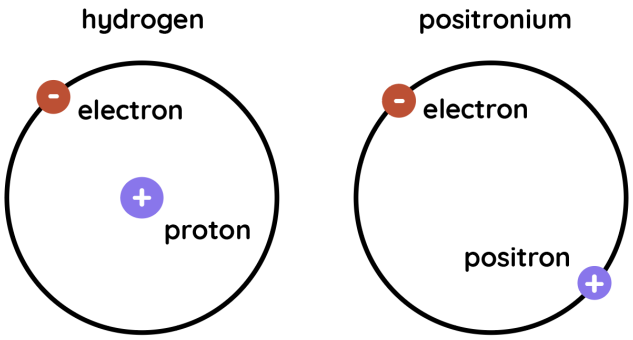

Figure 2.7: Comparison of hydrogen and positronium in Bohr's atomic model. Credit: based on Ghosh (2024)

Based on this model, the size of the two atoms can be calculated. After quantizing the angular momentum $L = n\hbar$ of Eq. (2.6) with the principal quantum number $n \in \mathbb{N}$, the orbital radius can be written as

$$r = r_n = \frac{4\pi\epsilon_0}{e^2 m}\hbar^2 n^2. \tag{2.13}$$

If we now calculate this distance for the hydrogen and positronium atom, bearing in mind that r_n is the distance between the two particles, we obtain $r_{\text{hydrogen}} \approx \frac{1}{2} r_{\text{positronium}}$. However, due to the equal mass of positron and electron, this distance characterizes the diameter of positronium. In the case of hydrogen, this distance is the radius due to the solid nucleus. This means that the true size of hydrogen and positronium is approximately the same. This also affects the frequencies of the photons emitted during transitions between the different energy levels. For comparable transitions, these frequencies are approximately twice as high as those of hydrogen. Using Eq. (2.12) to calculate the frequencies of potential recombination lines within the 2 GHz wide band between 13 and 15 GHz, four α recombination lines of hydrogen and three α recombination lines of positronium are identified in this range. These lines, along with their respective frequencies, are presented in Tab. 2.1.

Line	Frequency [GHz]
H79α	13.08885
Ps62α	13.47692
H78α	13.59549
H77α	14.12862
Ps61α	14.14514
H76α	14.68999
Ps60α	14.85827

Table 2.1: Expected recombination lines of hydrogen and positronium between 13–15 GHz and their corresponding frequencies.

Depending on the spin state of the two particles, there are two possible configurations for positronium: the so-called ortho-positronium (o-Ps) and the para-positronium (p-Ps). The lifetime of o-Ps is about 10^{-7} s before it annihilates into three photons, the lifetime of p-Ps is about 10^{-10} s before it annihilates into two photons (Deutsch, 1951). The 511 keV line, which will be discussed in more detail in Sec. 2.5.2, is observed during the annihilation of p-Ps.

2.5.1 Hyperfine Structure Transition [H I line]

Another way in which spectral lines can arise is through the hyperfine structure transition. This process results from the interaction between the spin of the atomic nucleus and the spin of the surrounding electrons (Scholz, 2018), which leads to a splitting of the energy levels V caused by the interaction of the magnetic moment μ of the nucleus with the magnetic field B

$$\Delta V = -\mu * B. \tag{2.14}$$

This is also the reason for the existence of the 21 cm emission line of hydrogen. It is created by a spin flip of the electron's spin, which is initially parallel to the proton, to an antiparallel configuration. This releases a photon with an energy of ~ 5.88 μeV. Following Carl R. Nave [2], this line not only serves as evidence for the presence of neutral hydrogen (H I) but is also a key

[2] http://hyperphysics.phy-astr.gsu.edu/hbase/quantum/h21.html

tool in studying the formation and composition of galaxies and nebulae, as it allows to map the distribution and motion of hydrogen gas, revealing insights into the structure, dynamics, and evolution of celestial objects. One of the first major discoveries made using the 21 cm line was the identification of the spiral structure of our galaxy (Liu & Chronopoulos, 2008).

2.5.2 Annihilation [511 keV line]

The decay of positronium occurs when the bound electron and positron interact and mutually annihilate, converting their mass into energy. This process is a direct consequence of Einstein's mass-energy equivalence,

$$E = mc^2. \tag{2.15}$$

Depending on the spin of the positronium, the annihilation results in the emission of either two or three photons.

For p-Ps, where the spins of the positron and electron are antiparallel, the annihilation produces two photons with an energy of 511 keV each. This specific energy corresponds to the rest mass of the electron (and positron) and results in the well-known 511 keV line (Jung et al., 2022). This line is of great significance as it serves as evidence for the presence of positronium, which in turn provides insights into potential dark matter. The following information is taken from Siegert (2023). The source of the 511 keV emission remains uncertain, with ongoing debates about whether it originates from the Galactic bulge, center, or disk. The annihilation rate observed is approximately $5 \times 10^{43}\,\mathrm{e^+ s^{-1}}$. Figure 2.8 shows a map of positronium annihilation in the Galaxy. The distribution of this emission is unusual, showing a luminosity ratio of bulge to disk of about 1, which does not match any known astrophysical source patterns. Identifying the exact source of these positrons and understanding the process of their annihilation are still significant challenges.

O-Ps, with parallel spins, decays more slowly and typically produces three photons due to conservation of angular momentum. These photons have a continuous energy distribution that is more difficult to observe compared to the discrete 511 keV line of p-Ps annihilation. In the radio regime of the electromagnetic spectrum, which is observed in the TELAMON project, the measured lines of positronium are primarily transitions between different energy levels. Since o-Ps is more stable and has a longer lifetime than p-Ps, the lines measured in the radio regime mainly originate from p-Ps.

2.6 Theoretical Radio Data Calibration

When radio data is measured with a telescope, the data usually needs to be converted from a non directly comprehensible unit (counts) into a physically meaningful flux density S to ensure the comparability of the individual measurements with each other. Therefore, the central point in the calibration of a source is the conversion from counts into the flux density with the unit Jansky, where

$$1\mathrm{Jy} = 10^{-23}\frac{\mathrm{erg}}{\mathrm{m^2\,Hz\,s}}. \tag{2.16}$$

As discussed by Burke et al. (2019), the measured flux density S depends on the received power P_ν, the effective area of the telescope A_{eff} and the sensitivity over the frequencies Δv and results in

$$S = \frac{2P_\nu}{A_{eff}\Delta\nu}. \tag{2.17}$$

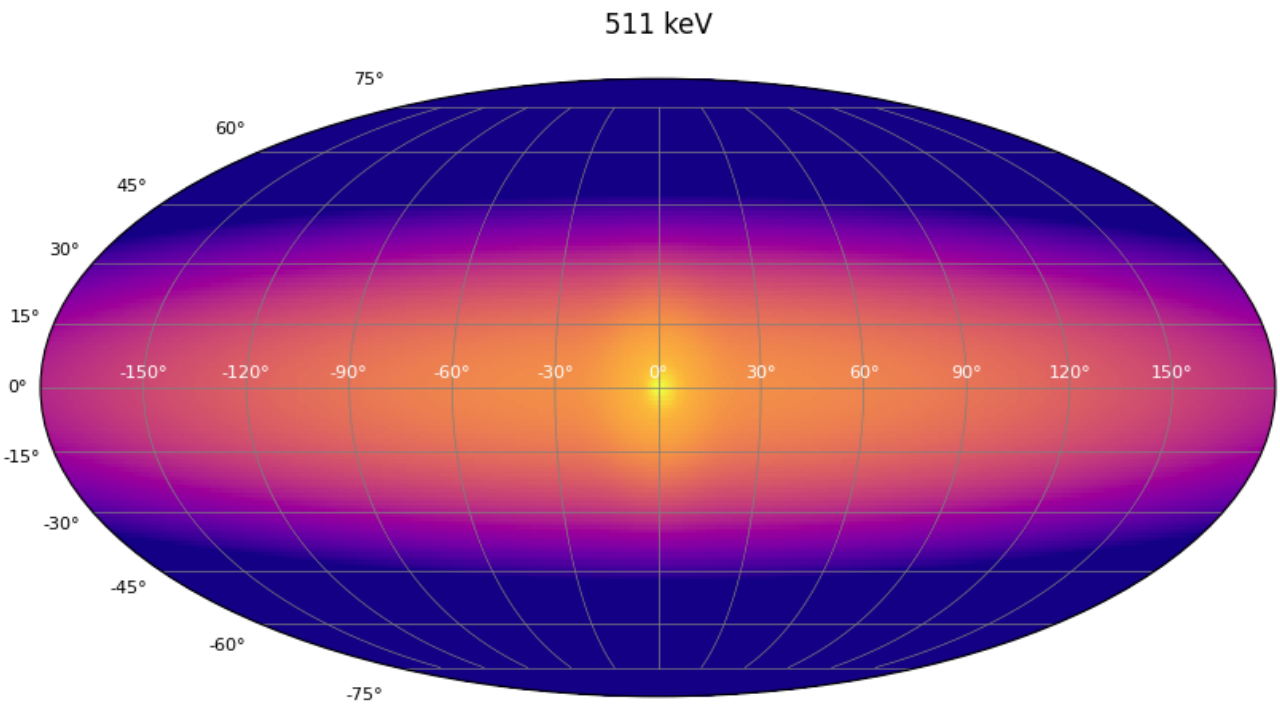

Figure 2.8: Positron annihilation in the Galaxy. Four-component model that describes the INTEGRAL/SPI data completely. Credit: Siegert et al. (2016)

For an ideal radio telescope the measured power P_ν depends on the effective area A_{eff} of the telescope, the brightness of the source B_ν and the power pattern of the antenna Π.

$$P_\nu = \frac{1}{2} A_{eff} \int_\Omega B_\nu(\theta, \Phi) \Pi(\theta, \Phi)\, d\Omega \tag{2.18}$$

The power pattern describes the directionality, which describes the sensitivity depending on the direction of the light. If the antenna is considered as a black body, the power it receives can be characterized by Planck's law. For radio frequencies, this can be simplified by the Rayleigh-Jeans approximation leading to

$$B_\nu = \frac{2\nu^2 k_B T}{c^2}, \tag{2.19}$$

where k_B describes the Boltzmann constant, T the temperature and c the speed of light. Assuming $\Pi(\theta, \Phi) \approx 1$, i.e., the power pattern is only sensitive to the light from the point source, Eq. (2.18) results in

$$P_\nu = \frac{1}{2} A_{eff} \int_\Omega \frac{2\nu^2 k_B T}{c^2} \Pi(\theta, \Phi)\, d\Omega = A_{eff} \frac{\nu^2 k_B T}{c^2} \Omega_A. \tag{2.20}$$

Using $\lambda = c/\nu$ and $\lambda^2 = A_{eff}\Omega_A$ determined by Rohlfs & Wilson (2013)

$$P_\nu = A_{eff} \frac{k_B T}{\lambda^2} \Omega_A = \frac{k_B T}{\lambda^2} \lambda^2 = k_B T. \tag{2.21}$$

Integrating over the frequency range $\Delta\nu$ and using Eq. (2.17), the flux density equals

$$S = \frac{2 k_B T}{A_{eff}}. \tag{2.22}$$

T is also known as the antenna temperature usually referred to as T_{Ant}, which is not corresponding to the physical temperature of the antenna but is rather the temperature a black body would have when emitting the power P_ν.

3 | Data Acquisition and Calibration

The calibration of the measurement data is the central task of this work and poses particular challenges. The aim of calibration is the comparability of the individual measurements with each other, but also of the individual amplitudes of the frequencies to each other. Calibration essentially involves converting arbitrary system units (counts) into physical units (Jansky). To ensure this, it is first necessary to understand how exactly the measurement data is recorded in order to then consider how to correct and convert the data. The aim of this work is to carry out a spectral analysis of the measured data in order to investigate the existence of spectral lines and thus to retrieve information about the composition of the observed sources.

3.1 Effelsberg 100m Radio Telescope

The following information is mainly based on information from Effelsberg Wiki[1] as well as information of the Max Planck Institute for Radio Astronomy (MPIfR)[2] website. The 100 m radio telescope in Effelsberg in Germany (see Fig. 3.1), which is operated by the MPIfR, is one of the largest fully steerable single-dish radio telescopes in the world with an antenna diameter of 100 m. With a surface accuracy of $\sigma = 0.5mm$ (rms), its instruments can detect radiation in a frequency range from $\sim$ 300 MHz ($\lambda \sim$ 90 cm) to $\sim$ 90 GHz ($\lambda \sim$ 3.5 mm). Gravity plays a significant role in telescopes of this size, deforming the dish differently depending on its orientation. Thanks to the principle of homology, the Effelsberg 100 m radio telescope always focuses the incoming light at one point despite this deformation. However, this point shifts depending on the alignment of the telescope. Figure 3.2 shows the beam path of the incoming radiation that hits the telescope. The incoming rays are first reflected by the dish and bundled into the primary focus and then concentrated further into the secondary focus. Both the primary focus and the secondary focus contain different receivers that can detect different wavelengths. By shifting the primary focus cabin, it is then always possible to find the point at which the beam is focused. The size of the telescope also has an important influence on its resolution. The angular resolution θ describes the angle at which two objects can just be distinguished from each other. This is represented by the Rayleigh criterion

$$\theta \approx \frac{\lambda}{D} \tag{3.1}$$

where λ is the observed wavelength and D is the diameter of the telescope. With the data used, where $\lambda \sim 2$ cm, this results in an angular resolution of $\theta \sim 0.7$ arcmin. To be able to observe as many points in the sky as possible, the telescope can be aligned in azimuth and elevation. The azimuth angle can be adjusted from 33.5° to 506.5°, the elevation angle from 8.1° to 89°. An azimuth angle of 0° corresponds to an azimuth direction to the North, one of 90° to an azimuth direction to the East.

[1] https://eff100mwiki.mpifr-bonn.mpg.de/doku.php
[2] https://www.mpifr-bonn.mpg.de/231173/specs

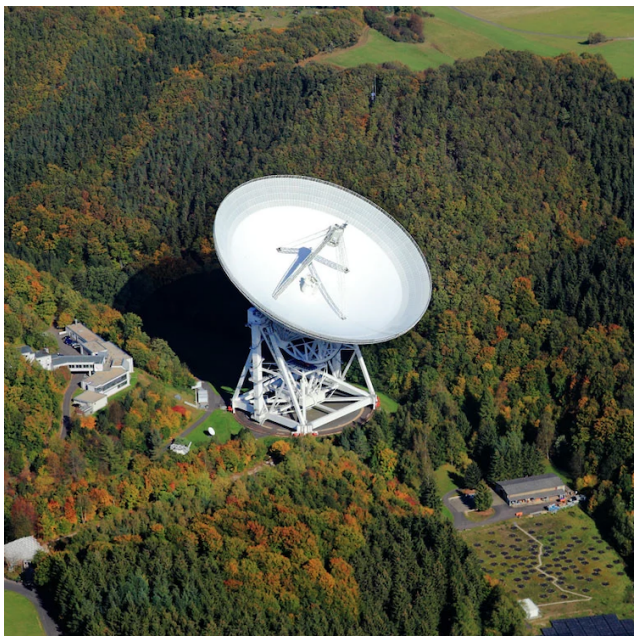

Figure 3.1: The 100 m radio telescope in Effelsberg Germany, operated by MPIfR Bonn. Credit: https://www.mpifr-bonn.mpg.de/337354/gallery

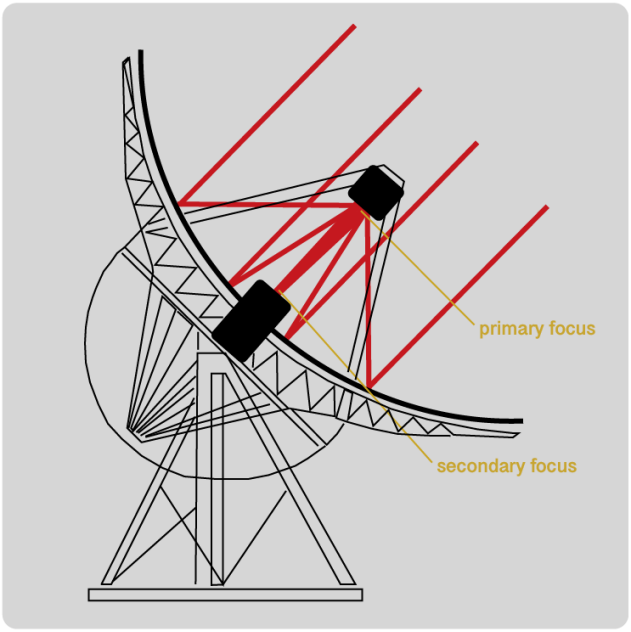

Figure 3.2: The path of incoming radiation for the Effelsberg 100 m radio telescope is shown. The radiation is first bundled to the primary focus and then further into the secondary focus. Credit: based on https://www.mpifr-bonn.mpg.de/57598/exploring_universe

3.2 Calibrating the TELAMON Data to Detect Spectral Lines

If a source is to be observed with the telescope, it is not possible to simply position the telescope and start recording immediately. Calibrator measurements must first be carried out in order to know the current properties of the telescope. This knowledge is then used to calibrate other sources. For longer observations lasting several hours or more, calibrator scans are repeated periodically to refine the telescope's focus and pointing, ensuring up-to-date calibration factors. Calibrator sources are sources whose properties are particularly well known, usually very bright sources that can be easily observed (Perley & Butler, 2017). In the TELAMON project NGC7027, 3C286 and W3OH are used. By utilizing these sources, the current focus point of the telescope is determined and, concurrently, the sensitivity of the receiver is calibrated. The focus is set by moving the secondary focus to the point of maximal amplitude. When the focus is set, a calibrator scan is recorded. This usually consists of several subscans, in the TELAMON project always 4 for the considered frequencies. For this purpose, the telescope performs cross-scans by moving in straight lines across the source in both the azimuth and elevation directions, starting and ending at small offsets from the source. A scan therefore not only consists of a stationary data point of a previously known location, but also has a time component that later plays a role in the calibration. Another point concerns the backend used in the telescope. In the TELAMON project, different backends are used: On the one hand, the continuum backend dual-spec-OPTOCBE and on the other hand, the spectro-polarimeter (SPECPOL) used for the data processing in this thesis. The SPECPOL backend records the 2 GHz-wide band with 1024 different frequency channels, resulting in a channel width of $\sim$1.95 MHz (Nguyen et al., 2021). Considering this, calibration factors can be calculated for each Calibrator source and then be used for the other scanned sources.

The calibration of the calibrator sources as well as the target sources involves three major

steps. The noise diode correction, the antenna temperature conversion and the final conversion into the flux density in Jansky, which will be explained in the following sections.

3.2.1 Noise Diode Correction

During the data acquisition process at the telescope, a noise diode with a known calibration temperature T_{cal} is periodically integrated into the circuit for every two data points to assist with the calibration of the antenna temperature conversion. This integration manifests as an amplitude alteration in the recorded measurement data. Consequently, two data points correspond to the measured amplitude, while an additional two data points reflect the measured amplitude plus the contribution from the noise diode. The difference d between these sets of points is determined, playing a critical role in the subsequent calibration step that converts counts to antenna temperatures. Figure 3.3 illustrates the impact of the noise diode on the measurement of amplitude over time for a specific frequency channel. Given that the noise diode is intermittently activated across all frequency channels, a correction must be applied individually to each channel. This correction involves calculating the difference between the values with and without the noise diode, which is subsequently subtracted from the timestamps associated with the noise diode. The resulting data is presented in Fig. 3.4, yielding a single curve representing amplitude over time.

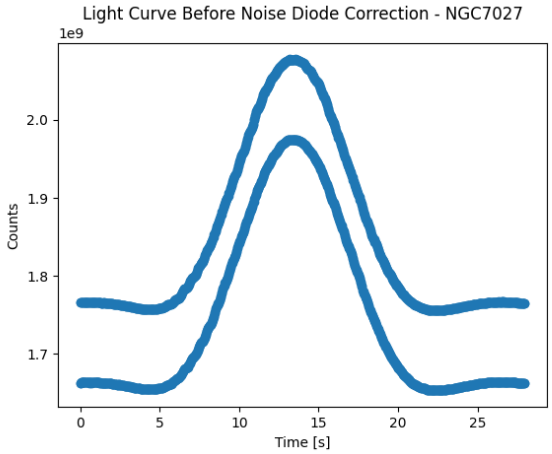

Figure 3.3: Measured signal of one scan (consisting of eight stacked and averaged subscans) of NGC7027 for one frequency plotted over time before noise diode correction.

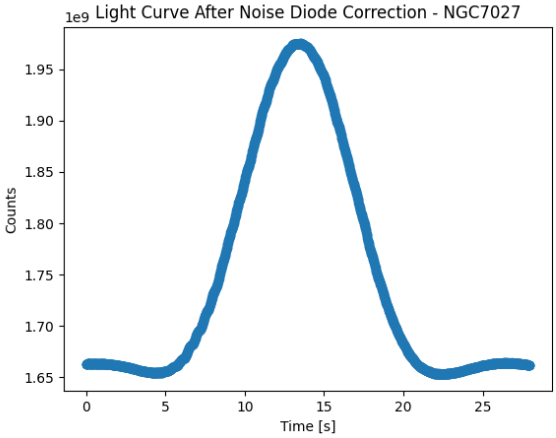

Figure 3.4: Measured flux density of one scan (consisting of eight stacked and averaged subscans) of NGC7027 for one frequency plotted over time after noise diode correction

3.2.2 Antenna Temperature Conversion

After correcting for the amplitude variations caused by the noise diode at each frequency channel, the conversion from counts to antenna temperatures can be executed. The objective of this conversion is to transform arbitrary count values to units of antenna temperature. Therefore, the measured counts $T_{obs[counts]}$ are transformed into antenna temperatures $T_{A[K]}$ with the unit Kelvin using the following equation:

$$T_{A[K]} = T_{cal[K]} \cdot T_{obs[counts]}. \tag{3.2}$$

The calibration process involves measuring the signal with the noise diode turned on and off (see Fig. 3.3). The difference in counts between these two measurements (see Fig. 3.5) corresponds to the calibration temperature T_{cal}, but expressed in units of counts. The known T_{cal} value in

Kelvin from the Effelsberg Wiki is then used to determine a conversion factor between counts and Kelvin.

Note that T_{cal} is frequency dependent. For simplicity, the average T_{cal} value over the 2 GHz-wide band, as provided in the Effelsberg Wiki, is applied. This approach is justified because an additional, more accurate flux calibration is performed using calibrator observations.

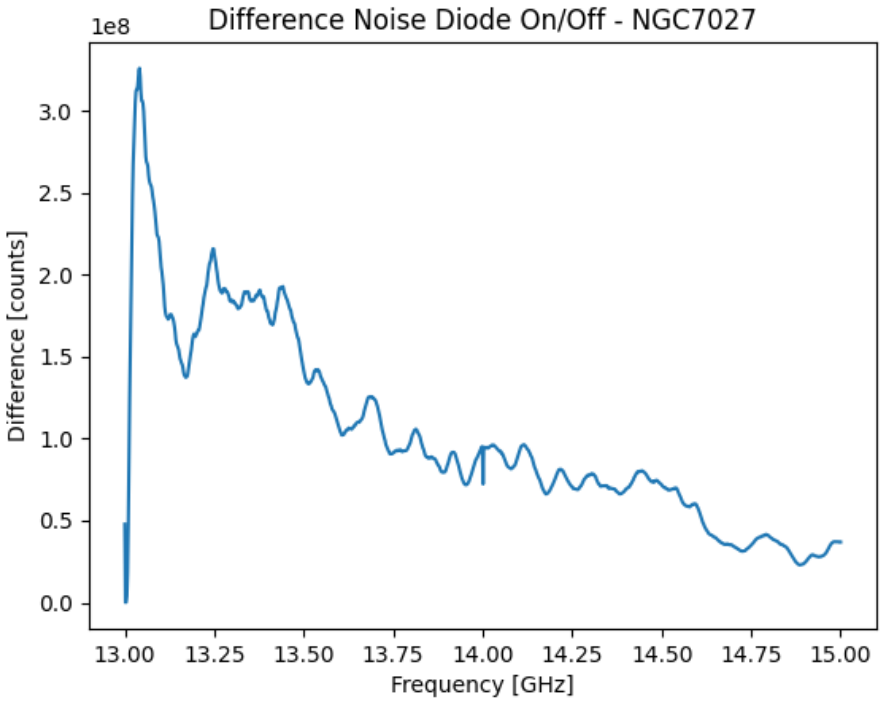

Figure 3.5: The calibration temperature measured of NGC7027 is plotted over the frequency. The frequency dependence can clearly be seen. The deviation observed at ∼13 GHz is attributed to data disturbances in this range. Credit: Effelsberg Wiki

3.2.3 Absolute Flux Calibration

In the conversion of antenna temperatures from Kelvin to Janksy, the procedure differs for the first time between calibrator sources and target sources. Using the Calibrator sources, calibration factors are determined. These are values used to convert Kelvin to Jansky and are applied to each frequency channel. For the target sources, this conversion is straightforward because the calibration factors previously determined with the calibrator sources are simply multiplied with the values in Kelvin. This step is slightly different for calibrator sources, as here the calibration factors have to be calculated. To determine the flux densities of the calibrator sources in Jansky, one could use Eq. (2.22) in theory stating that

$$S = \frac{T_{Ant}}{\frac{A_{eff}}{2k_B}} = \frac{T_{Ant}}{\frac{\eta_A A_{geom}}{2k_B}} = \frac{T_{Ant}}{\Gamma}. \tag{3.3}$$

The effective area A_{eff} can be written as a product of the geometric area and the aperture efficiency η_A. Combined with a factor including the Boltzmann constant $(2k_B)^{-1}$, this is called the sensitivity Γ. According to Kraus (2007), η_A is a product of multiple other efficiencies such as surface inaccuracies η_{surf}, aperture blocking η_{bl} and tapering η_{tap}. Therefore, the flux density in Jansky can not be determined in a trivial way. This is why usually a model of the source is used to convert the antenna temperatures from Kelvin into the flux density in Jansky.

The models for NGC7027, 3C286 and W3OH are taken from Zijlstra et al. (2008), Perley & Butler (2017) and Eppel et al. (2024) respectively. To determine a calibration factor through the model, the ratio of model and measurement is formed at each frequency, adjusting the measured value to the model.

$$calfactor(\nu) = \frac{model(\nu)}{measurement(\nu)} \tag{3.4}$$

As there is no reason to believe that the brightness of a source is recorded identically by each frequency channel, each channel requires separate calibration. However, this approach poses the risk of calibrating out any lines since the model, as shown in Fig. 3.6 on the left, follows a simple power law (Eq. (2.3)) and does not account for any lines that might already be present in the calibrator spectrum. However, because the positronium recombination lines might also appear in the calibrator sources, calibrating each frequency individually would map the expected lines into the calibration factors, making them no longer visible in the result.

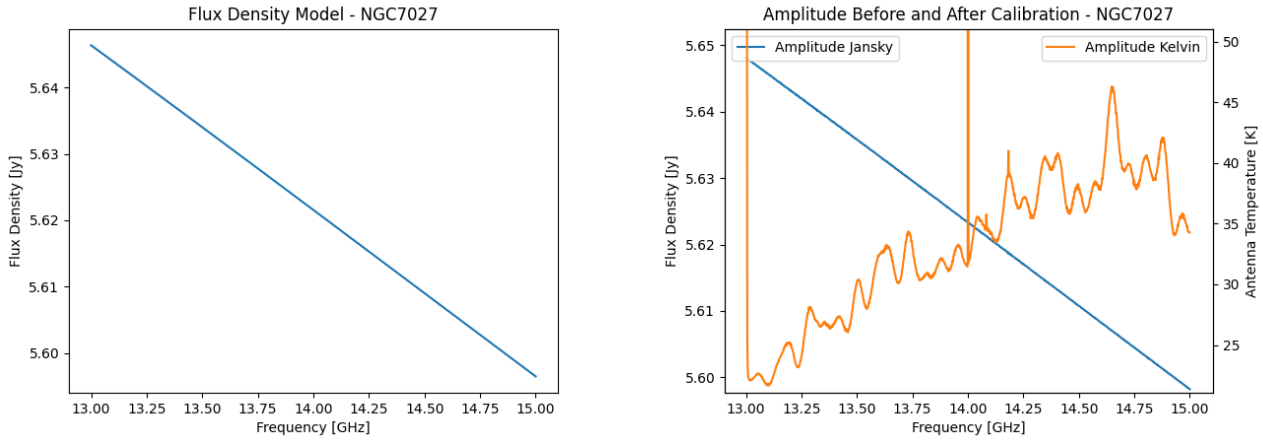

Figure 3.6: Flux model of NGC7027 between 13 – 15 GHz following a power law (left), along with the calibrated amplitudes of NGC7027 shown before and after amplitude calibration (right).

To address this issue, a moving average is applied across the Gaussian-fitted data prior to calibration, which incorporates neighboring frequencies into the calibration factor. A challenge arises from individual frequencies with large outliers, as these can affect the calibration factors of neighboring frequencies. To minimize this influence while preventing lines from being calibrated out, the averaging factor is set to ∼10 channels, as the line width is expected to range between 3–5 channels. This decision is further supported by the fact that there are no significant outliers within a 10-channel range of the anticipated positronium lines, as the averaging would distort the regions around the outliers and therefore affect the positronium lines.
Another important point to address is the model itself. As the model is used to calibrate the flux density, i.e. the amplitude of the sources, it initially seems very logical to divide the amplitude of the model by the measured amplitude in order to arrive at the calibration factor. To determine the amplitude of the measurement, each frequency is considered individually over time. A Gaussian is then fitted to the data and the amplitude is determined from this. Since an integration over time is performed to look at the spectral lines (i.e. the intensity is shown versus frequency), this approach assumes that the areas correlate with the amplitudes. Testing this, the amplitudes of the measurements match those of the model as intended, shown in Fig. 3.6 (right). However, examining the mean flux density across frequencies after calibration reveals, as seen in Fig. 3.7, that this does not align with the model. To understand this discrepancy, it is necessary to consider how Fig 3.7 is generated. The plot of the measured data shows the

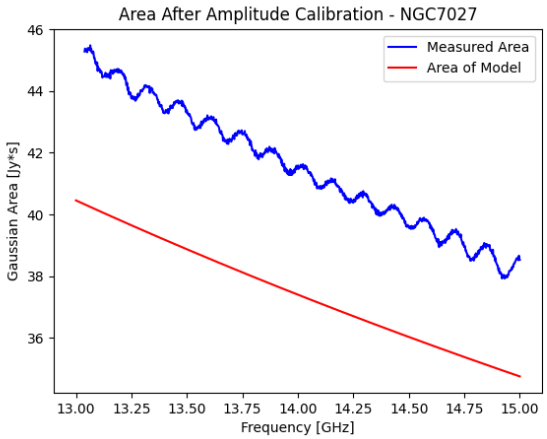

Figure 3.7: A comparison between the calibrated Area of one scan (after calibrating the amplitudes) of NGC7027 and the calculated Area of the Model is shown.

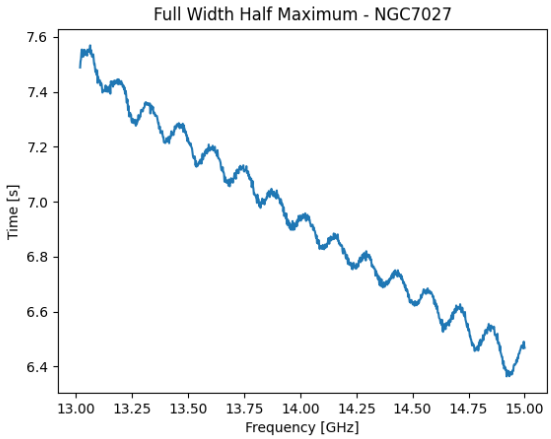

Figure 3.8: FWHM of the Gaussian fits for one scan of NGC7027. This illustrates the chance of the width of the Gaussian depending on the frequency. Disturbances (at around 13, 13.3 and 14.2 GHz) are filtered out.

mean flux density at each frequency, calculated as the average over time for each frequency. If the model does not match the measurement, yet the Gaussian amplitude does, the cause lies in a variation in the Gaussian width. This fluctuation is also evident in the full width half maximum (FWHM) plot shown in Fig 3.8.

This problem is also described in Winkel et al. (2012) and two possible solutions are presented, namely position and frequency switching. However, both involve steps that have to be taken into account during data acquisition. In the TELAMON project, this was not taken into account in the previous measurements, which is why these two methods cannot be used here. To compensate for this variation in the width of the Gaussian, the calibration is performed according to the area of the Gaussian. Then the area of the model is divided by the area under the Gaussian curve at each frequency. Without the averaging described above, the calibration via the area also manages to eliminate the variations of the surfaces integrated over time. However, since the moving average must be performed in order not to lose spectral lines, the variations are still visible.

A final step is required to ensure that the calibration factors can be correctly applied to the data: the deduction of the baseline. The baseline describes the system temperature, i.e., the temperature measured by the system when not pointing at a source. It is important to note that the baseline correction performed here agrees very well with the known system temperature of the receiver (34K) found in the Effelsberg Wiki as shown by the nearly identical difference between Figures 3.9 and 3.10. Fig. 3.9 shows the spectrum before baseline removal and therefore the background noise is still included, in Fig. 3.10, this background is removed. This reduction is performed by modeling the background level with a linear fit and the astrophysical signal with a Gaussian fit, allowing the background to be subtracted from the signal.

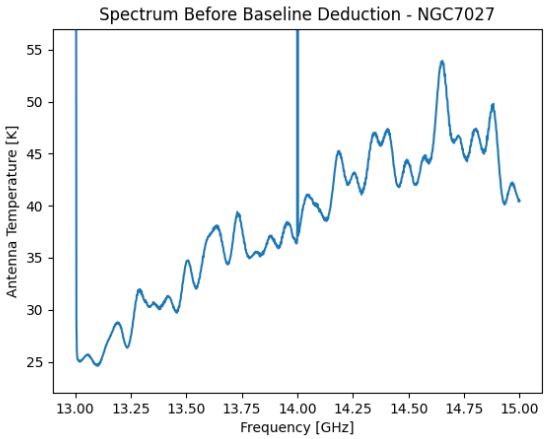

Figure 3.9: Mean flux density versus frequency for NGC7027 converted into antenna temperatures without deduction of the baselines for each frequency.

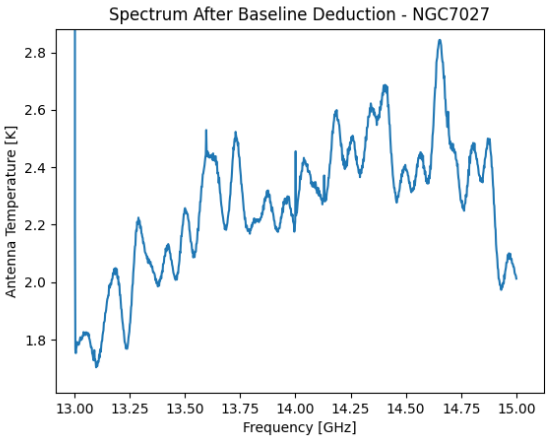

Figure 3.10: Mean flux density versus frequency for NGC7027 converted into antenna temperatures with deducted baselines for each frequency.

3.3 Improved Calibration

In this section, several methodological choices, potential issues, and errors encountered during the calibration process are addressed. These include why certain steps, such as converting antenna temperatures, are necessary, or why down-sampling can improve the results. Furthermore, adjustments made to handle variations and artifacts in the data are outlined.
First, the initial processing of the data is to be discussed. It is important to note that the recording of the data starts earlier than the movement of the telescope. However, since the duration of a scan is precisely known (25 seconds), the actual start of the measurement can be calculated.
The next step addresses the intermediate conversion to antenna temperatures. As stated above, the conversion from Kelvin to Jansky is performed by

$$data_{[Jansky]} = calfactor \cdot data_{[Kelvin]} = \frac{model}{data_{[Kelvin]}} \cdot data_{[Kelvin]}. \tag{3.5}$$

When using a model, it should not matter whether the calibration factor is determined directly from the counts or from the antenna temperatures. However, this is only the case if the difference between data with and without the noise diode is constant over time. The Effelsberg Wiki shows that this difference varies for measurements taken at different times for the same source[3]. Therefore the calibration step of the antenna temperatures can't be neglected.

[3] https://eff100mwiki.mpifr-bonn.mpg.de/doku.php?id=information_for_astronomers:rx:s20mm

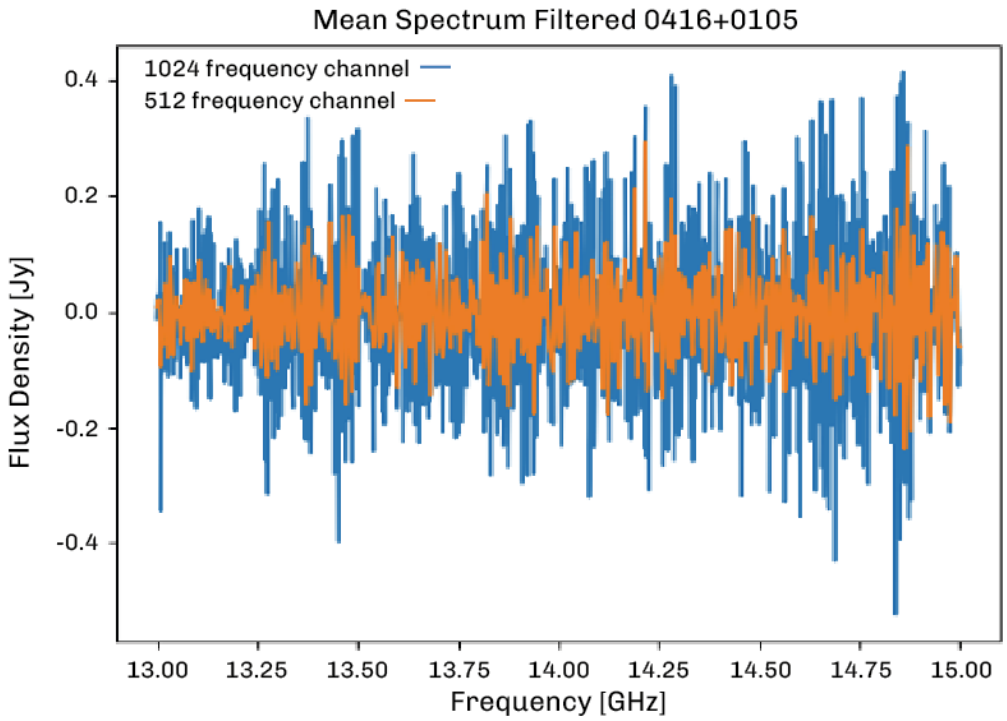

Figure 3.11: Flux density versus frequency in the region of 0416+0105. After calibration the time component of the spectrum is stacked and averaged and filtered with the Savitzky-Golay filter. Both with 1024 frequency channels (blue) and down-sampled to 512 frequency channels (orange).

The third point, which requires further examination, aims to enhance the calibration outcome with regard to the search for spectral lines. It is divided into two parts.

The first part entails the down-sampling of the data from 1024 frequency channels to 512 frequency channels. This results in a reduction of noise by a factor of $\sqrt{2}$, or approximately 29% shown in Fig. 3.11. Consequently, the integration range of a frequency channel is doubled. However, given that the width of the emission lines from positronium is estimated to span several channels, this approach proves beneficial.

The second part deals with the filtering of the data using the Savitzky-Golay filter, which creates the possibility to remove the disturbances described in Winkel et al. (2012) in the best possible way by fitting a polynomial of the nth degree

$$y = a_0 + a_1 x + a_2 x^2 + ... + a_n x^n \tag{3.6}$$

and minimizing this to determine the best fit:

$$\text{Minimize} \left[\sum_{i=-m}^{m} (y_{k+i} - \sum_{j=0}^{p} a_j x_{k+1}^i)^2 \right]. \tag{3.7}$$

Additionally, the filter removes the continuum emission from all sources, leaving only the spectral lines and any remaining noise in the signal.

3.4 Stacking of Radio Data

After calibrating the measured data using the calibration factors from the calibrator sources, the final step is to reveal the spectral lines by stacking multiple scans. The measured data for each scan can be described as the sum of the underlying signal $S(\nu)$, represented by the spectral line, and a noise component of the j-th scan, represented by the variable $n_j(\nu)$:

$$x_j(\nu) = S(\nu) + n_j(\nu). \tag{3.8}$$

Here $n_j(\nu)$ is random noise with a mean value of 0, distributed symmetrically around this mean.

The process of stacking involves overlaying of individual scans, with the aim of reducing the random noise and enhancing the signal. The stacked signal is then calculated as $\bar{x}(\nu)$:

$$\bar{x}(\nu) = \frac{1}{N}\sum_{j=1}^{N} x_j(\nu) = S(\nu) + \frac{1}{N}\sum_{j=1}^{N} n_j(\nu). \tag{3.9}$$

N describes the number of scans. As the noise components are uncorrelated, their variance in the stacked signal reduces proportionally to $1/N$:

$$\mathrm{Var}\left(\frac{1}{N}\sum_{j=1}^{N} n_j(\nu)\right) = \frac{\sigma_n^2}{N}. \tag{3.10}$$

Here σ_n^2 is the variance of the noise for each scan. This leads to a reduction in the noise amplitude by a factor of $\sqrt{N}$:

$$\sigma_{\bar{n}}(\nu) = \frac{\sigma_n}{\sqrt{N}}. \tag{3.11}$$

This means that a spectral line that was previously weaker than the noise becomes more visible by increasing the number N of stacked scans.

3.5 Radio Frequency Interference

Radio Frequency Interference (RFI) refers to unwanted signals from external sources that contaminate radio frequency bands, leading to inaccuracies in data collected during observations. The 13–15 GHz frequency range used in the TELAMON project, in general does not have a lot of RFI compared to other frequency bands measured in the TELAMON project. However, in some scans RFI is present nonetheless. One example for this is shown in Fig. 3.12, where RFI is seen in the frequency range of 14.5–14.75 GHz. These disturbances can significantly impact the quality of the data, as they obscure the desired astronomical signals. To mitigate the effect of RFI, statistical filtering techniques can be employed. For example, outliers can be identified and removed based on the mean and standard deviation of the signal, allowing for the exclusion of invalid data points caused by interference. By applying such filtering methods, the reliability of the measurements can be improved, ensuring more accurate results for the analysis of astrophysical sources.

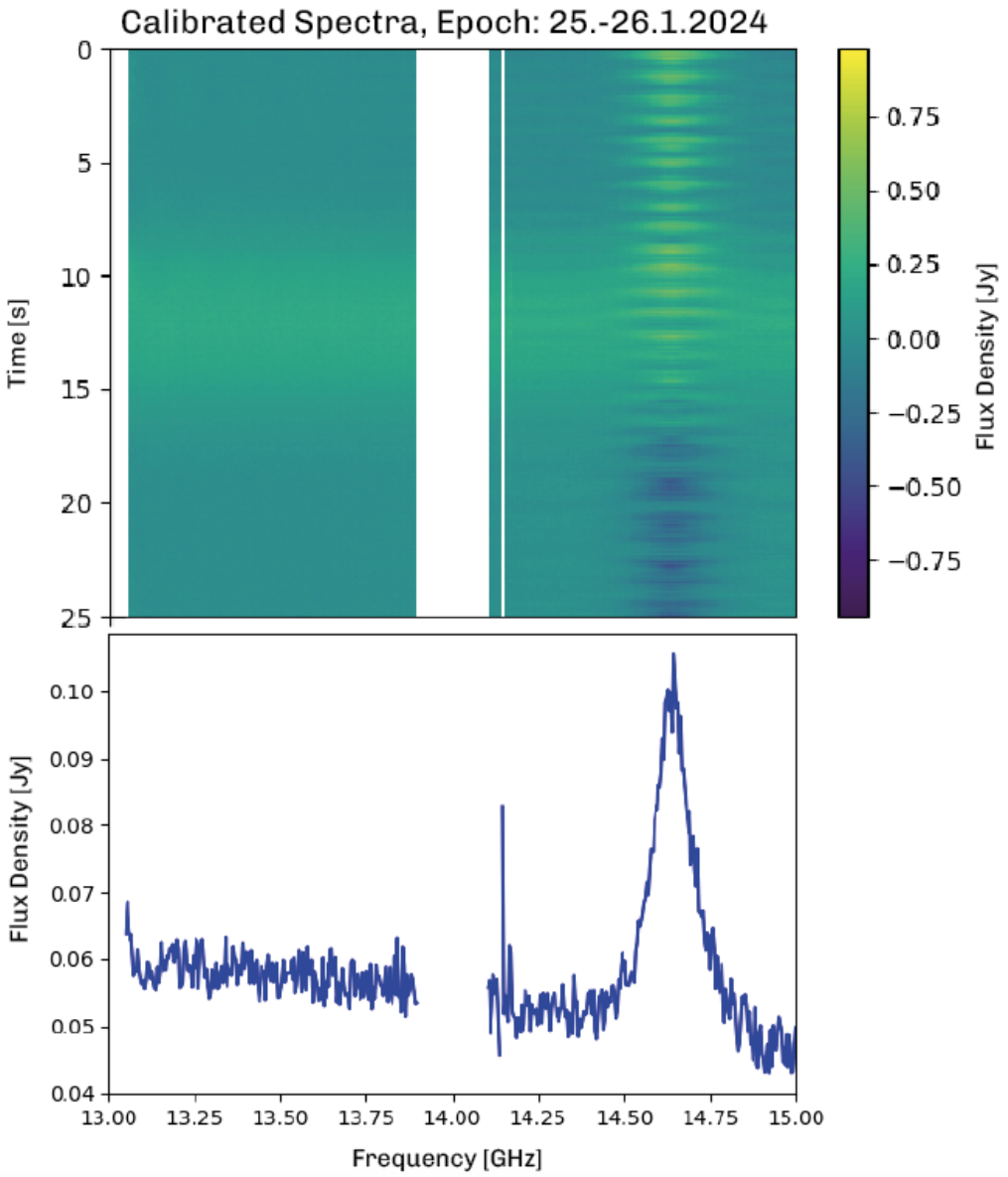

Figure 3.12: All target scans from the epoch of January 25–26, 2024 are combined and averaged. The recorded data are plotted both as a time-frequency intensity map, with the intensity represented by color (top), and as an integrated spectrum over time showing intensity over frequency. RFI is evident in the range between 14.5–14.75 GHz, clearly visible in both plots.

3.6 Line Significance and Upper Limit Determination

Once the data has been calibrated and overlaid, it is important to be able to say with certainty, based on objective criteria, whether or not there is a significant spectral line detected at a given frequency. If there is no significant line detected, upper limits for the specified frequency can be calculated. This is achieved through hypothesis testing, where two system-adapted models are statistically compared (Bevington & Robinson, 2003). One model m_0 describes a straight line with intersect a and slope b:

$$m_0(\nu; a, b) = a + b\nu, \tag{3.12}$$

The other model m_1 adds to this straight line a Gaussian with the area F (corresponding to the flux), the expected frequency of the line ν_0 and the line width σ:

$$m_1(\nu; a, b, F) = a + b\nu + \frac{F}{\sqrt{2\pi}\sigma} \exp(-\frac{1}{2}\frac{(\nu - \nu_0)^2}{\sigma^2}). \tag{3.13}$$

To compare the two models with each other, χ^2 is calculated in each case. For the first model χ_0^2 results in:

$$\chi_0^2 = \sum_{i=1}^{N_{data}} \frac{(d_i - m_{0i}(\nu; a, b))^2}{\sigma_i^2} \tag{3.14}$$

d_i represents the measured value at position i, N_{data} denotes the total number of data points, and σ is the uncertainty at the corresponding frequency. Since calculating the uncertainties for individual frequencies is non-trivial, the standard deviation of the entire curve is used instead. Similarly, χ_1^2 is calculated via

$$\chi_1^2 = \sum_{i=1}^{N_{data}} \frac{(d_i - m_{1i}(\nu; a, b, F))^2}{\sigma_i^2} \tag{3.15}$$

using model 1 instead. To compare the two models with each other, the parameters a, b and F are varied and it is determined which of these two models represents the data best. This is done by calculating the difference $\Delta\chi^2 = \chi_0^2 - \chi_1^2$. In practice, a fit is performed for the values a and b and only F is varied over a certain range. The resulting plot of $\Delta\chi^2(F)$ over the changed flow F can then be used to estimate the significances, their uncertainties or the upper limits for a specified frequency.

4 | Results

This chapter presents the results of the data processing. The aim is to search for spectral lines of positronium or derive upper limits if no significant lines can be determined. Prior to this, it is first important to understand and verify the calibration so that the calibration solutions can later be applied to the target sources. Therefore, the results for the individual calibrator sources are presented first, followed by the results for all target sources.

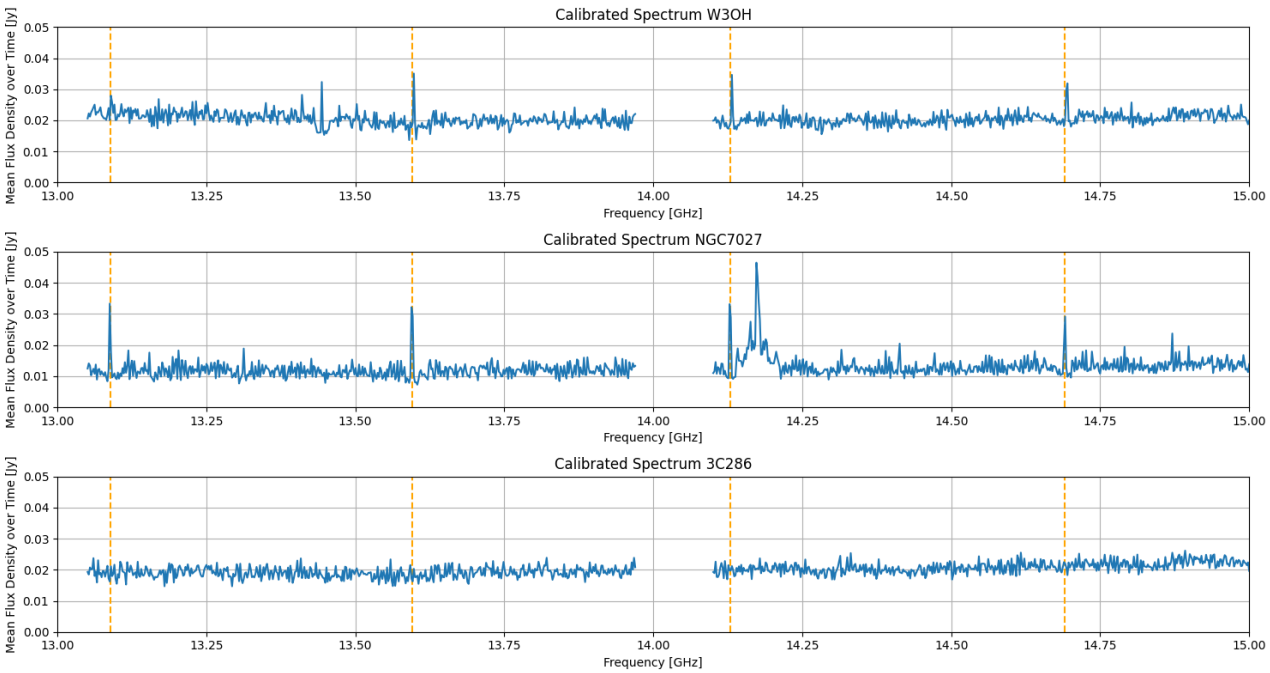

Figure 4.1: Calibrated residual spectra of the three calibrator sources W3OH, NGC7027, and 3C286, with the continuum emission filtered out using the Savitzky-Golay filter. The resulting residual emission, revealing the spectral lines on top of the power-law source, is shown as the mean flux density versus frequency. The calculated frequencies for the hydrogen lines H79α – H76α are marked as vertical orange dotted lines, from left to right. Frequency ranges with RFI, specifically 13 – 13.05 GHz and 13.9 – 14.1 GHz, were discarded.

The plots in Fig. 4.1 show residual spectra of the three calibrator sources that were processed and calibrated according to Sec. 3.2. Each of the three plots shows eight subscans, which were first integrated over the subscan duration to create one spectrum per subscan. These individual spectra were then averaged to produce a final, averaged spectrum. Furthermore, all three spectra were filtered using a Savitzky-Golay filter (from the SciPy package) with a window size of 35 and a polynomial order of two. This filtering helps reduce variations in the full width half maximum (FWHM) described in the previous chapter and allows for a more consistent comparison of the spectra based on the noise. As mentioned earlier, the Savitzky-Golay filter also removes the continuum emission of all sources, resulting in the "residual spectrum", which ideally only contains spectral lines and (sky) background noise. It is noticeable that in two of the three sources (NGC7027 and W3OH) increased amplitudes can be seen at the calculated

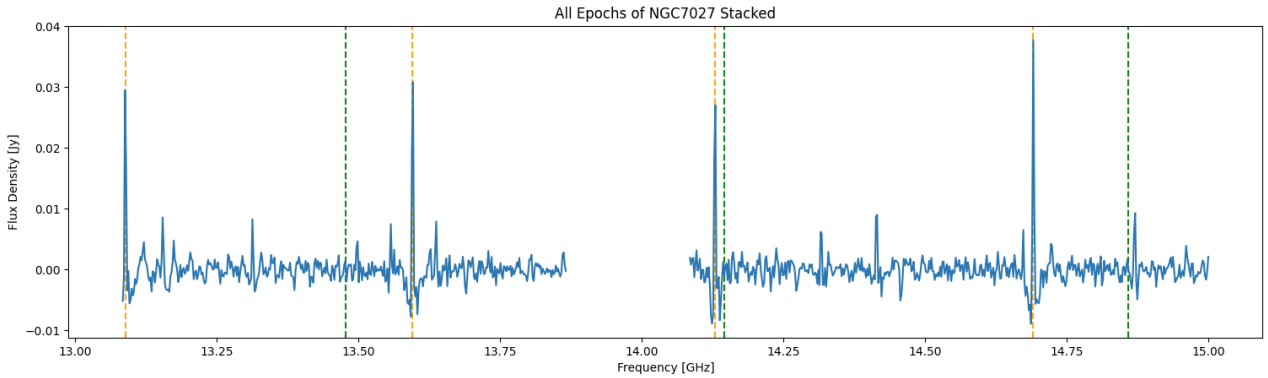

Figure 4.2: Calibrated spectra of NGC7027 for all epochs superimposed. The mean flux density is shown versus frequency. The dotted orange lines represent the calculated frequencies for hydrogen, while the green lines indicate the corresponding frequencies for positronium lines. In order to preserve calibration accuracy, frequency ranges with higher interference, specifically 13 – 13.05 GHz and 13.9 – 14.1 GHz, were discarded.

frequencies of the hydrogen lines H79α – H76α. The peak at ∼14.2 GHz in NGC7027 can be classified as RFI. This becomes evident when examining a scan from a different time period (see Fig. A.1). In contrast, no increased amplitudes can be recognized in the spectrum of 3C286. In order to enable a more precise examination of the hydrogen lines and to obtain confirmation of the accuracy of the calibration, Fig. 4.2 shows an overlay and averaging of the scans of all epochs for NGC7027. It can be clearly seen that the noise is reduced by stacking and the amplitudes at the spectral lines of hydrogen become much more visible.

The significances of the hydrogen lines can be read from Fig. 4.3, where $\Delta\chi^2(F)$ is plotted against the flux. The maxima of the curves can be used to determine the significances for the hydrogen lines shown in Tab. 4.1. The significance of the four expected hydrogen lines ranges from $\sim 12\sigma$ for $H79\alpha$ to $\sim 24\sigma$ for $H76\alpha$. For a comparison with W3OH, see Fig. A.2. However, due to better data for NGC7027, NGC7027 will be considered in the following.

Line	$\Delta\chi^2_{\text{max}}$	**Significance** (σ)	**Amplitude [mJy]**
H79α	140	~ 12	39
H78α	468	~ 22	44
H77α	370	~ 20	40
H76α	576	~ 24	41

Table 4.1: Maximum $\Delta\chi^2$ values and their corresponding significances for hydrogen lines in NGC7027 as well as the measured amplitudes.

Figure 4.4 displays the calibrated spectra of the target sources. Here, the individual spectra were stacked and averaged, followed by integration and averaging over time. This process allowed the mean flux density over time to be plotted against frequency. Figure 4.4 shows the plot before applying the Savitzky-Golay filter (top) and after filtering (bottom). Before filtering, both the absolute values of the mean flux density and certain amplitude fluctuations are noticeable. Especially, there is an increase in flux density around the calculated hydrogen recombination line H76α at 14.69 GHz, as well as near the calculated spectral line for positronium Ps61α at 14.15 GHz. After applying the Savitzky-Golay filter, these fluctuations are no longer visible. However, compared to the scans of the calibrator sources, a significant reduction in noise is evident. This noise reduction was achieved partly through the stacking and averaging of 1715 individual scans and partly by down-sampling the data from 1024 to 512 frequency channels.

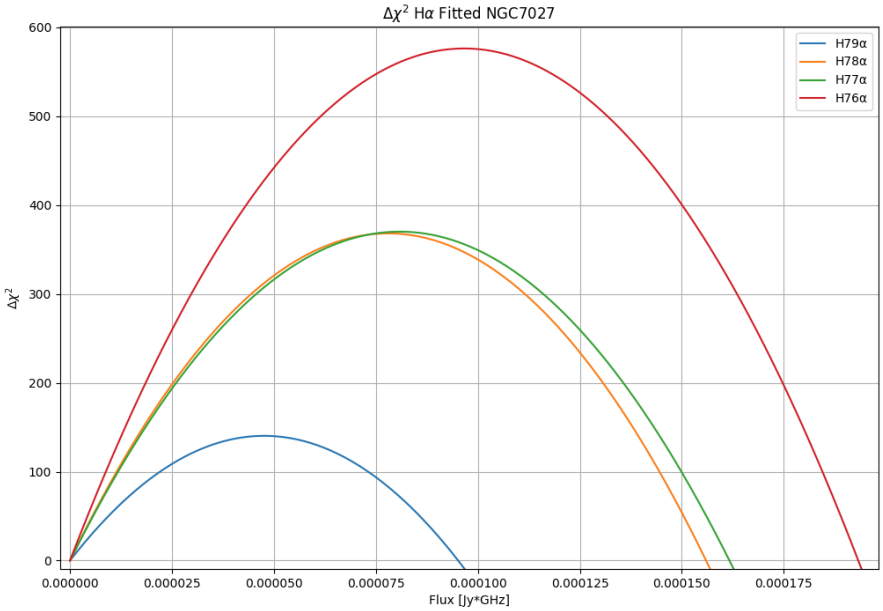

Figure 4.3: $\Delta\chi^2(F)$ plotted over the flux for all four hydrogen lines within the frequency range of 13-15 GHz. Comparing the two models χ_0^2 (linear approximation) and χ_1^2 (linear approximation with Gaussian added). The maxima of the curves represent the significance of the specified spectral line of hydrogen.

Using the radiometer equation[1]

$$\mathrm{SNR} = \frac{T_A}{T_{\mathrm{sys}}}\sqrt{\Delta\nu\tau}, \tag{4.1}$$

the theoretically expected noise for the combined measurements can be calculated. The signal-to-noise ratio (SNR) describes the ratio between the signal S and the noise N. Here, T_A represents the measured values as antenna temperatures in Kelvin, T_{sys} denotes the system temperature, $\Delta\nu$ is the frequency range of a single channel, and τ is the total integration time of all scans. Rearranging the equation to isolate the noise leads to

$$N = \frac{S}{T_A} T_{\mathrm{sys}} \left(\Delta\nu\tau\right)^{-1/2}. \tag{4.2}$$

Substituting the values used in Fig. 4.4 yields a theoretical noise level of 0.062 mJy. In comparison, the measured noise level in Fig. 4.4 is 0.21 mJy. This deviation is within the expected range and is primarily due to the uncertainties mentioned in Chap. 3.

To determine whether positronium lines are present in the spectrum, the maxima of the $\Delta\chi^2$ curves for the respective lines can be examined (Fig. A.3, A.4, A.5). However, it is evident that all maxima are significantly below a value of 1 and therefore, far from the 3σ threshold, which would require a value of at least 9. Consequently, upper limits are calculated for the positronium lines.

The upper limits for the positronium lines, calculated as described in Sec. 3.6, are presented in Tab. 4.2. Two approaches were applied, referred to as "single" and "combined" method. Both use the previously explained calculation with the help of two models, where one model describes a straight line and the other the straight line with corresponding Gaussian. In the "single" approach, this calculation is performed individually for each potential spectral line. In the "combined" approach, the second model is modified to include multiple Gaussian functions, with one Gaussian centered at the frequency of each expected line, fitting them simultaneously.

$$m_2(a, b, F) = a + b\nu + \sum_{i=1}^{N_{lines}} \frac{F \cdot f_i}{\sqrt{2\pi}\sigma} \exp(-\frac{1}{2}\frac{(\nu - \nu_i)^2}{\sigma^2}). \tag{4.3}$$

[1] https://radio.astro.gla.ac.uk/ralectures/pw/radiometer.pdf

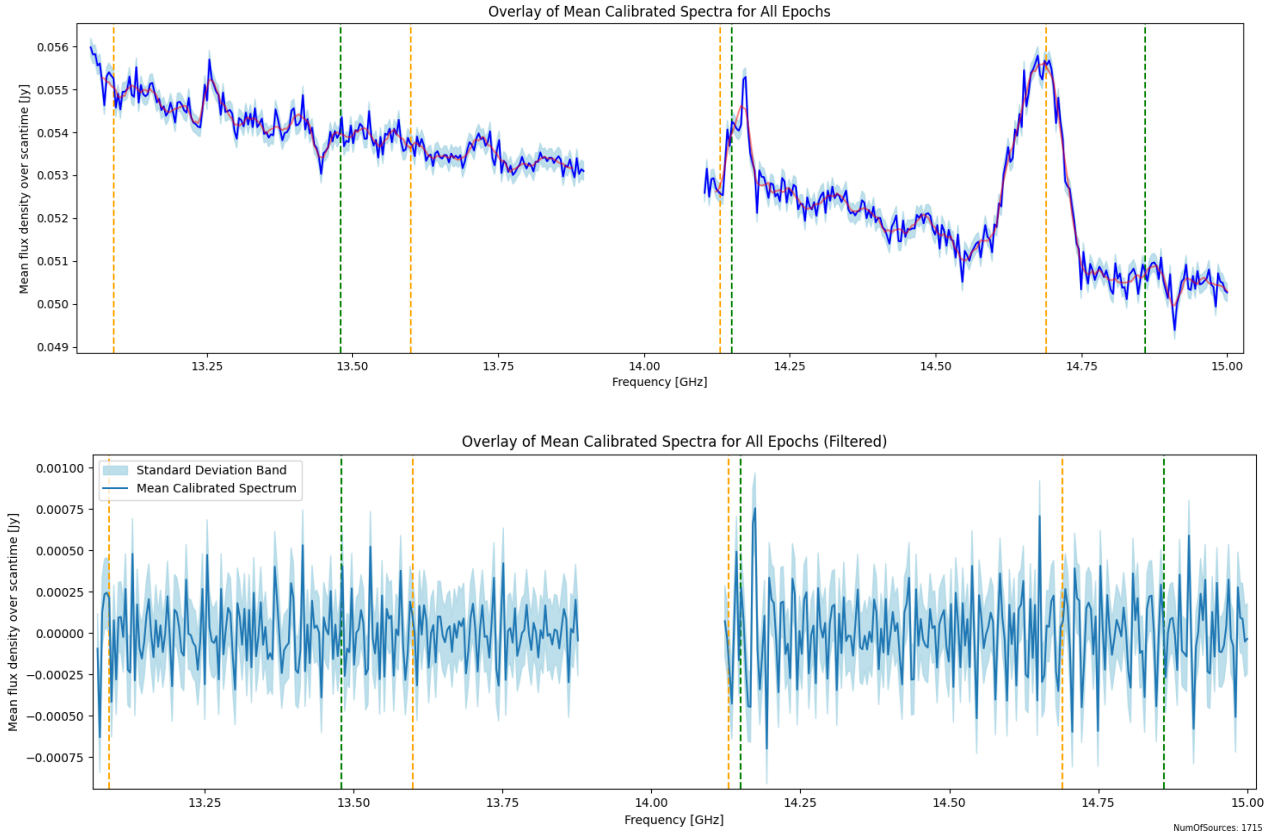

Figure 4.4: Calibrated target sources for all epochs superimposed. The upper plot shows the mean flux density versus frequency, averaged over time, before applying the Savitzky-Golay filter. The lower plot displays the same data after the Savitzky-Golay filtering. The dotted orange lines represent the calculated frequencies for hydrogen recombination lines, while the green lines indicate the corresponding frequencies for positronium lines. The red line in the upper plot represents the fitted Savitzky-Golay filter. In both plots, frequency ranges with RFI, specifically 13 – 13.05 GHz and 13.9 – 14.1 GHz, were discarded to preserve calibration accuracy. Similarly, the peak at ∼14.2 GHz and at ∼14.65 GHz can be classified as RFI, comparable to Fig. 3.12 and Fig. A.1.

ν_i corresponds to each expected frequency of a line, N_{lines} describes the total number of lines in the given frequency band and f_i is a factor referring to the calculated expected flux of the respective line (Thomas Siegert, priv. comm.).

The results for the 3σ upper limits for the amplitudes of the positronium lines are as follows: Using the "single" method for all epochs of NGC7027 combined, the upper limits range from $\mathbf{5.1-7.2\,mJy}$. In contrast, the "combined" method for the same source yields upper limits of $\mathbf{3.6-4.0\,mJy}$.

For all target sources overlaid (using the "combined" method), which includes data from 1715 scans, the 3σ upper limits for Ps62α – Ps60α are $\mathbf{0.6-0.7\,mJy}$. The larger number of scans in this case leads to a significantly lower noise level and therefore smaller upper limits.

These values are determined using the $\Delta\chi^2$ method, as described in Sec. 3.6, and are visualized in Fig. A.3, A.4 and A.5, where $\Delta\chi^2$ is plotted against the flux F. The upper limits are derived from the area under the Gaussian curves. To obtain the upper limits for the amplitudes, the amplitude of the Gaussian can simply be used.

Figure 4.5 displays the results for the 3σ upper limits of the expected positronium spectral lines, as well as the flux of the hydrogen lines determined by Gaussian fitting, including the corresponding uncertainties.

Method	**Line**	**3σ Flux** $10^{-20}\,\mathrm{erg\,cm^{-2}\,s^{-1}}$	**3σ Amplitude** mJy
Single Model NGC7027	Ps60α	17.9	7.2
	Ps61α	12.8	5.1
	Ps62α	15.9	6.4
Combined Method NGC7027	Ps60α	10.0	4.0
	Ps61α	9.5	3.8
	Ps62α	9.0	3.6
All Sources Overlaid	Ps60α	1.6	0.7
	Ps61α	1.6	0.6
	Ps62α	1.5	0.6

Table 4.2: Upper limits for Positronium for NGC7027 and all stacked target sources. The 3σ flux is considered as the area under the fitted Gaussian at the specific frequency, the 3σ amplitude describes the corresponding amplitude.

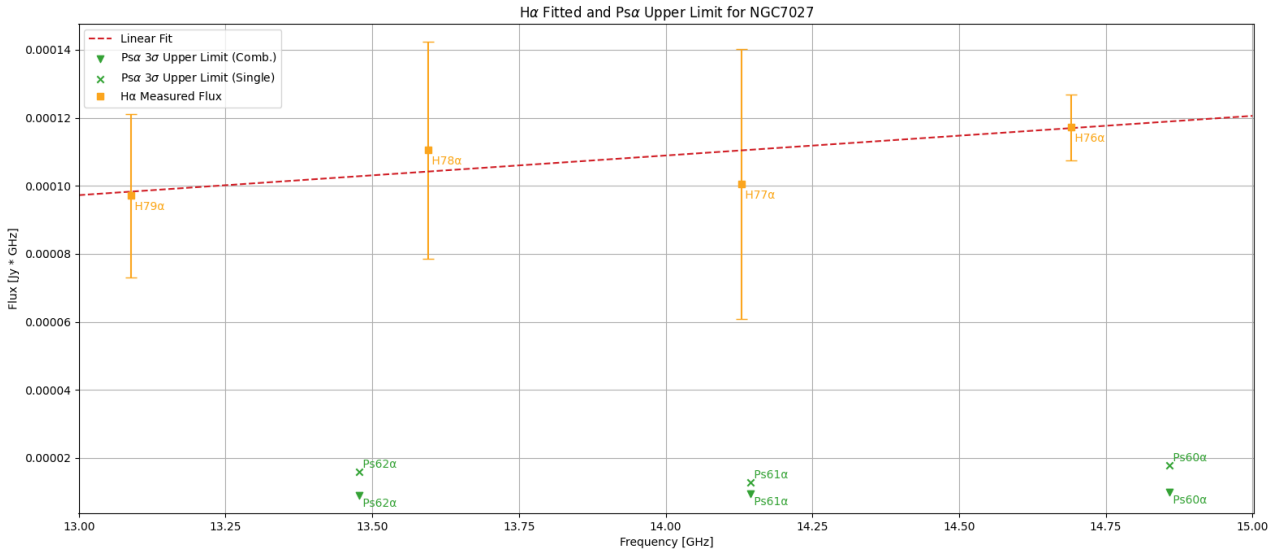

Figure 4.5: A Gaussian with $\sigma \approx 10\,\mathrm{MHz}$ is fitted for each Hα line. The area of the fitted Gaussian, plotted in orange, indicates the flux at the frequency of the respective spectral line. To test the consistency of the results with the theoretical model, which predicts a slight increase in flux across the lines, hydrogen lines are used as a reference. The red dotted line, representing a linear fit weighted by the uncertainties, is plotted to show this trend. Since the red line remains within the error bars of the measured flux values, this demonstrates agreement between the measurements and the theoretical prediction. In green, the 3σ upper limit is shown for both the "single" and "combined" methods for Psα in NGC7027.

5 | Discussion and Analysis of Uncertainties

In the following, the measurement results are examined in more detail to better understand the reliability as well as the limitations of the current approach. Subsequently, potential sources that increase uncertainties of the measurements and possible issues with the applied method are analyzed.

While the search for positronium in the radio regime has been pursued in earlier research (e.g. Staveley-Smith et al. (2022)), this thesis introduces a new method providing further insights. Staveley-Smith et al. (2022) used the ultra-wide band receiver of the Parkes Telescope to stack 20 and 26 different Psα lines pointing at 47 Tucanae (47 Tuc) and Omega Centauri (ω Cen) respectively. In contrast, the method presented in this thesis concentrates on a much narrower frequency range between 13 and 15 GHz in which there are only three potential Psα lines, but uses significantly more individual scans that are stacked and averaged. Compared to the results of Staveley-Smith et al. (2022), who estimated upper limits of 1.7 mJy for 47 Tuc and 0.8 mJy for ω Cen, the upper limits obtained in this thesis for an individual source (NGC7027) are higher with 3.6 – 4.0 mJy. However, the values derived from the combined analysis of all scans, which yield an upper limit of 0.6 – 0.7 mJy, are lower. Improving the upper limits using the method applied in this thesis does not demonstrate the superiority of one method over the other. The quality of the results primarily depends on the number of lines or scans included. The improvement observed here is therefore mainly attributable to the larger dataset available for this thesis.

In order to validate the method, three artificial lines were inserted into the spectra before calibration at 13.25, 13.5, and 13.75 GHz. These three lines have a peak amplitude of $5 \cdot 10^5$ counts. The unit in counts is used because the lines are added prior to calibration, as they are intended to test the calibration. Converted to Jansky, this corresponds to a line strength of < 0.01 Jy in a single scan. The width of the lines is 1 MHz. The results presented in Fig. 5.1 demonstrate the clear presence of these lines after calibration, stacking and filtering even though their initial amplitudes before calibration did not exceed the noise level. Assuming the negligible redshifts of the source regions, this represents an important step toward advancing the search for positronium recombination lines in the radio regime. The fact that different redshifts can have an influence on the result is due to the fact that the stacked source scans originate from different regions in the sky and therefore have different redshifts. This can lead to a broadening of the line, which was not taken into account in this bachelor thesis and would of course also have an influence on the expected amplitude of the lines. There are also other potential sources of uncertainty, the influence of which, however, can be assessed as having varying degrees of impact. Probably the most relevant point here plays a role directly in the last step of the calculation of the upper limits. This is the variance σ used for the calculation of χ^2. This actually represents the uncertainty of each individual data point, but is formed in a simplified manner from the standard deviation of the complete measured data. Both the points of potential recombination lines and other frequencies classified as interference are removed. As the variations described in Sec. 3.2.3 also have a major influence on the standard deviation, the data is first filtered using the Savitzky-Golay filter. The influence of the parameters used

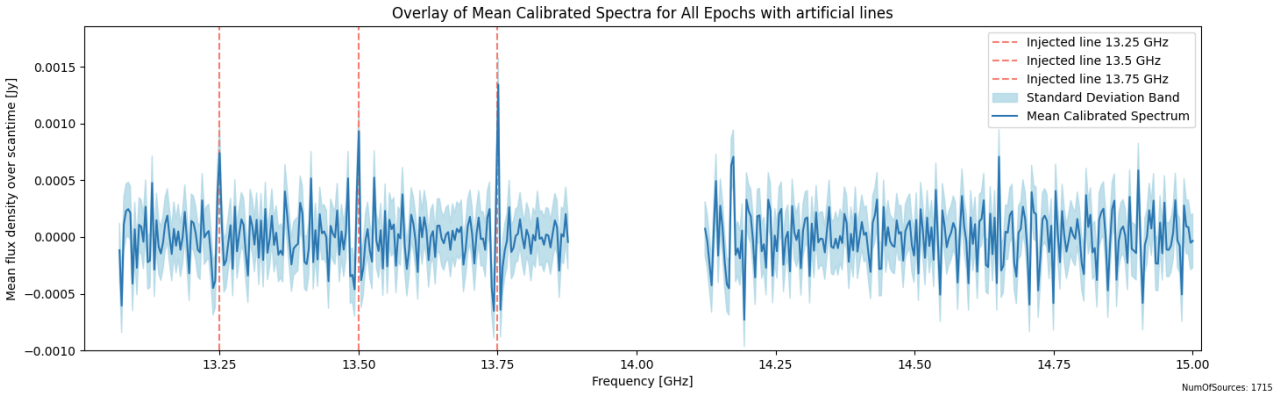

Figure 5.1: Mean calibrated spectrum of all overlaid target sources is plotted over the frequency. Before calibration three artificial recombination lines with a peak amplitude of 5×10^5 counts ($<$0.01 Jy) and width $\sigma = 1$ MHz are added at 13.25 GHz, 13.5 GHz and 13.75 GHz. Although these lines initially did not exceed the noise level, they become clearly visible after calibration. In order to preserve calibration accuracy, frequency ranges with higher interference, specifically 13 – 13.05 GHz and 13.9 – 14.1 GHz, were discarded.

for the Savitzky-Golay filter on the standard deviation is shown in Fig. 5.2. It is clear that the filtering has a major impact on the standard deviation. However when looking at the outcome $\Delta\chi^2$ shown in Fig. 5.3, a limit can be determined at $\Delta\chi^2 \sim 2$. This justifies the value used for the filter with a window size of 35 and a second degree polynomial.

Another step in the calibration process that may contribute to uncertainties is the averaging described in Sec. 3.2.3. This has an influence on the neighboring frequencies and results in changes. An outlier in the data thus produces an attenuation of the neighboring frequencies. For the expected lines of positronium, this will probably be negligible, as it had no significant effect on the measured hydrogen lines either, as they are many times stronger than the expected lines for positronium in the target sources.

In addition, there are some minor points that do not directly distort the result, but nevertheless explain why the results are in a certain range. A major challenge with the TELAMON data is RFI. In order to filter individual sources with particularly strong RFI, a basic standard deviation-based iterative filter was used. In addition, the outlier detection algorithm called Inter-Quartile Range Mitigation (IQRM) from Morello et al. (2022) was tested. However, both were only partially successful as seen in Fig. 5.4. The filter based on the standard deviation did not manage to recognize all disturbances and IQRM filtered out the lines first instead of the disturbances in a test with the calibrator source NGC7027 and was therefore also unsuitable.

Due to the inability to implement this filtering method, scans with significant disturbances had to be completely discarded. This naturally has a negative impact on the stacking of the data, as considerably fewer datasets are available. Furthermore, in the overlay of all target sources between 14.1 GHz and 14.2 GHz, as well as between 14.6 GHz and 14.75 GHz, the issue of unresolved smaller disturbances becomes clearly visible. Since these disturbances occur in many of the available scans, they accumulate and result in noticeable variations in the flux in the overall plot. Even when attempting to address this using the Savitzky-Golay filter, it inevitably distorts the results in the specific regions.

Another important aspect to consider, in addition to the Psα lines, is the analysis of the hydrogen lines measured in the two calibration sources NGC7027 and W3OH. To address this, it is necessary to determine whether the flux density of the lines yields expected values and whether they originate from the sources themselves or from a region between the observer and the source.

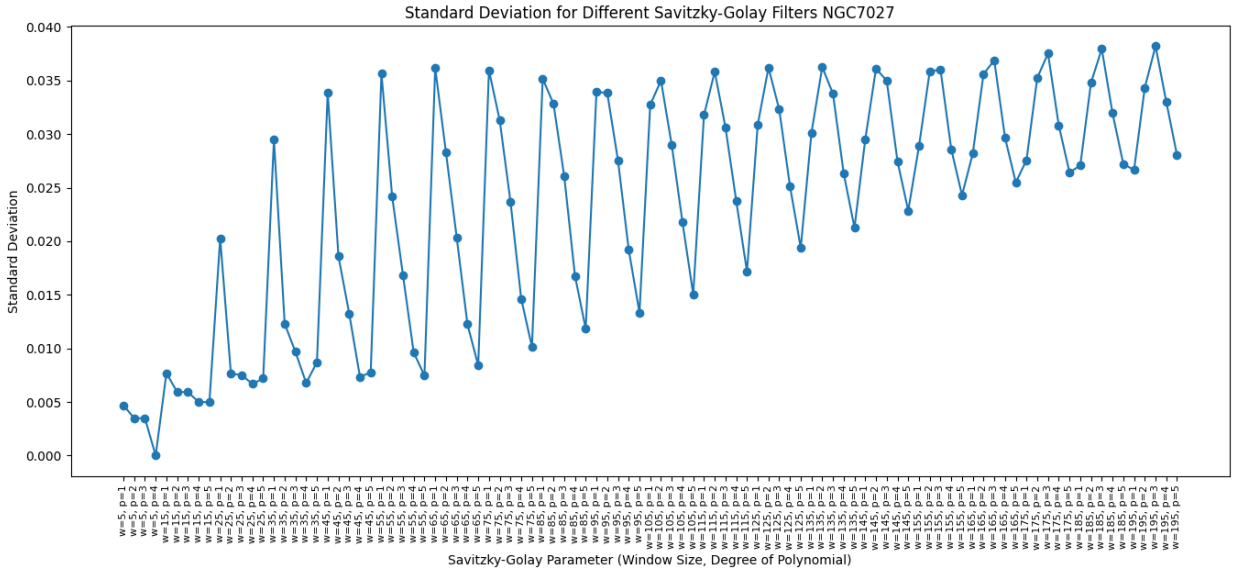

Figure 5.2: The standard deviation is plotted versus different window sizes and degrees of polynomials of the Savitzky-Golay filter. It can be seen that the different parameters have a major impact on the standard deviation.

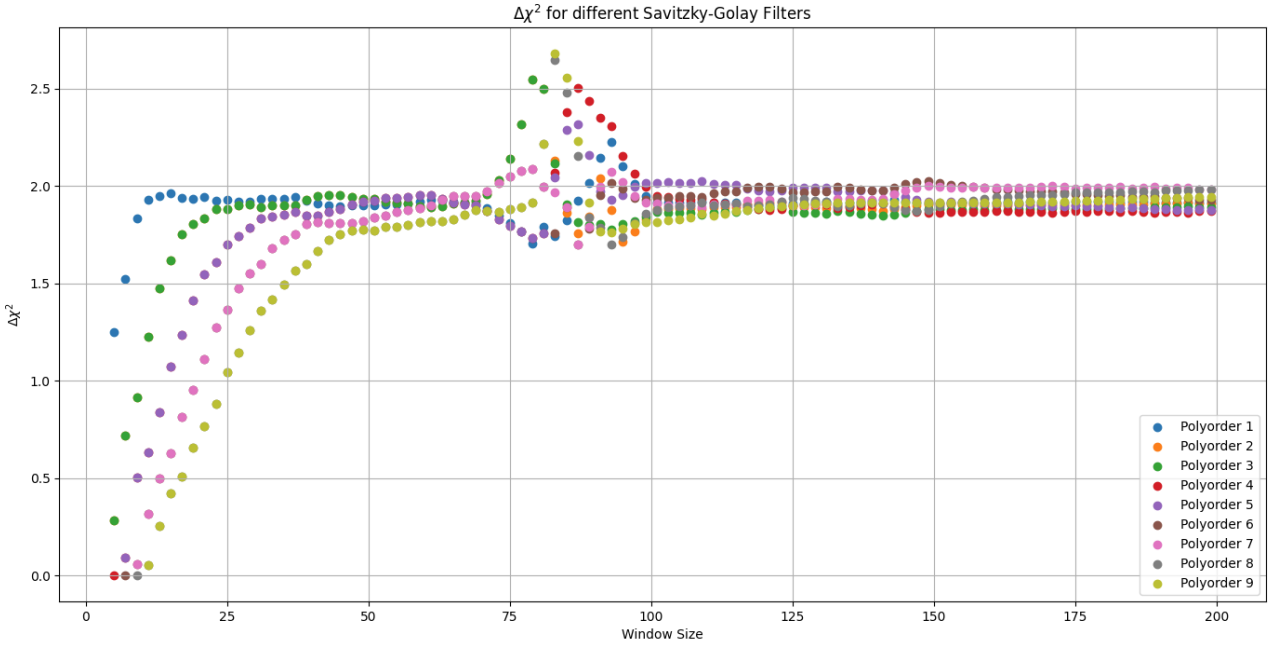

Figure 5.3: $\Delta\chi^2$ plotted versus window size, one of the two Savitzky-Golay parameters. The other parameter, represented by different colors, indicates the order of the fitted polynomial. The significant variation in χ for a window size between 70 and 100 arises due to an outlier at the lower frequency edge. In this range, the outlier prevents a Gaussian fit to the H79α line, thereby distorting the results.

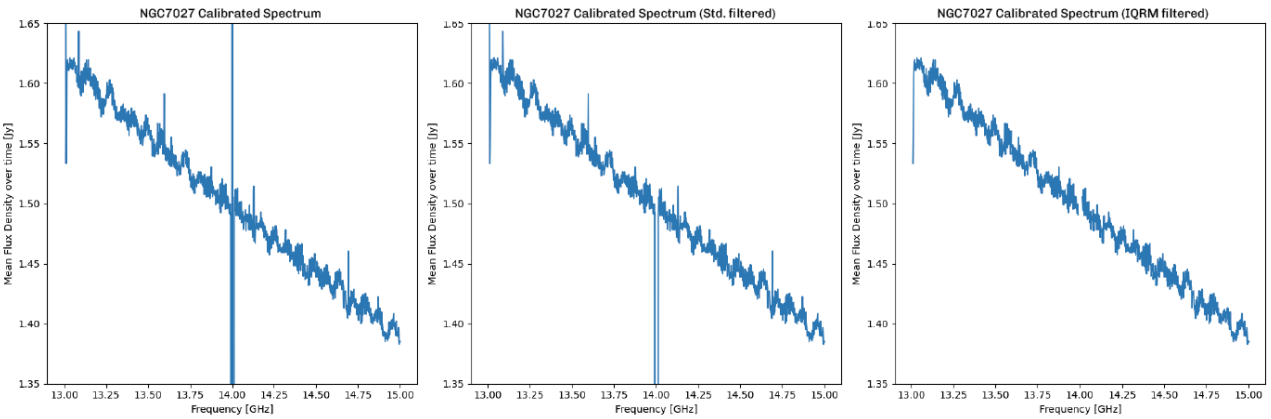

Figure 5.4: The mean flux density over time versus frequency is plotted for NGC7027 comparing two different types of filtering. The (left) plot depicts the calibrated spectrum without filtering. The (middle) plot the spectrum with the applied standard-deviation filter and the plot on the (right) has the IQRM filter applied. At around 13 GHz and 14 GHz there is interference that needs to be filtered out. The other protruding amplitudes represent the recombination lines of hydrogen and must not be removed by the filter.

For the frequencies of the four hydrogen lines (13.09 GHz, 13.60 GHz, 14.13 GHz and 14.69 GHz), TELAMON data show amplitudes ranging between 39 mJy and 44 mJy for NGC7027. Chaisson & Malkan (1976) examined the H76α line of NGC7027 and reported an antenna temperature of $\sim$0.04 K. Converting this with Eq. (2.22) and approximating A_{eff} with $(\pi D^2)/4$ (Condon & Ransom, 2016) where D equals the diameter of the NRAO telescope (42.7 m), this corresponds to a flux density of $\sim$70 mJy, which is higher than the measurements in this thesis. This can likely be explained by the fact that, for the calculation in my thesis, integration was performed over the observation time during the cross-scans. Even though the outer regions were excluded, the measured flux density does not exactly correspond to the actual value and will always be lower.

To further validate the origin of these lines, Chaisson & Malkan (1976) provided a detailed analysis demonstrating that the hydrogen recombination lines arise directly from NGC7027. One critical argument is the compact size of NGC7027, which ensures that the observed line broadening effects, such as Stark broadening, are intrinsic to the source and not influenced by interstellar turbulence or other intermediate effects. Specifically, the authors noted that planetary nebulae like NGC7027 remain "entirely pointlike for any single-dish radio observation" and that variations in line width as a function of the principal quantum number n are consistent with the plasma density ($N_e \approx 10^{4.7}\,\mathrm{cm}^{-3}$) expected for the nebula.

Furthermore, Chaisson & Malkan (1976) confirmed that the line profiles match Voigt functions, which are characteristic of Doppler and Stark broadening at the nebular electron temperature of $\sim 14,000$ K. This agreement between observed and theoretical line shapes strengthens the conclusion that the detected lines are intrinsic to NGC7027. Additional tests on baseline stability with unrelated sources showed no indication of contamination from intermediate regions.

A final point to address is the significance of the detected lines. With significances of $12-24\,\sigma$, all four measured Hα recombination lines surpass the three-sigma threshold.

Therefore, it can be stated that the hydrogen lines measured are highly likely to be real and originate from NGC7027 itself.

6 | Conclusion and Outlook

In this thesis, a method was presented that demonstrates how recombination lines can be searched for using existing radio data, even if their amplitudes in individual measurements are significantly smaller than the noise. To achieve this, data collected in the TELAMON project between 2021 and 2024 were stacked and averaged, effectively reducing the noise. Although recombination lines from positronium were not directly detected, upper limits for the flux and the amplitudes of these lines were calculated for both the individual source NGC7027 and all target sources combined. In the measured 2 GHz wide band between 13 GHz and 15 GHz, the three recombination lines of positronium Ps60α – Ps62α are theoretically present at 14.86 GHz, 14.15 GHz and 13.48 GHz. The combination of all target sources yields upper limits of 0.6 – 0.7 mJy.

To confirm the feasibility and effectiveness of this method, artificial recombination lines at three different frequencies were added before calibration. The fact that they are clearly visible after calibration demonstrates the functionality and robustness of this method. Additionally recombination lines of hydrogen are visible in two of the three calibrator sources NGC7027 and W3OH (H79α – H76α). For NGC7027, the measured intensity of the lines are $\sim$ 40 mJy, with detection significances ranging from 12 to 24 σ. That said, potential issues have to be addressed as well. For instance, due to different sky directions and the resulting redshifts, the recombination lines may appear smeared, making them weaker and broader than expected. Additionally, RFI in the data poses significant challenges.

Therefore, future work could focus on specific regions of the sky to eliminate issues related to varying redshifts. Moreover, developing an effective algorithm to mitigate RFI would be beneficial. Such an algorithm should reliably detect interference at individual frequencies without filtering out actual lines. It would also be advantageous to extend filtering to the time domain to identify interference that occurs only during part of the observation period. This approach could substantially increase the number of usable data samples, leading to improved noise reduction and, consequently, greater sensitivity. Furthermore, performing a gain curve calibration and applying an opacity correction are further methods to significantly enhance the accuracy of the results, leading to more precise outcomes.

Finally, combining the method used in this work with the approach employed in Staveley-Smith et al. (2022) could yield further improvements. In Staveley-Smith et al. (2022), data are recorded using the ultra-wideband receiver at the Parkes telescope, which covers a broad frequency spectrum. Individual lines within this large range are stacked to enhance sensitivity. Similarly, the TELAMON project records data not only in the 13–15 GHz range but also across various other bands between 5.3 GHz and 45 GHz. Future research could focus on exploring these additional bands, as well as stacking data not only from individual bands over four years but also by combining measurements from all observed bands simultaneously. The two methods could therefore be combined. In total, 23 recombination lines from Ps43α to Ps84α are available within the recorded bands of the TELAMON project. This would significantly enhance sensitivity, potentially enabling the direct detection of positronium recombination lines in the radio range in the future.

Bibliography

Antonucci R., 1993, In: Annual review of astronomy and astrophysics. Vol. 31 (A94-12726 02-90), p. 473-521., 31, 473

Appenzeller I., 2012, Introduction to astronomical spectroscopy. Vol. 9, Cambridge University Press

Beckmann V., Shrader C., 2012, Active Galactic Nuclei. Wiley-VCH, Weinheim

Bekhti N. B., et al., 2016, Astronomy & Astrophysics, 594, A116

Bertone G., Hooper D., Silk J., 2005, Physics reports, 405, 279

Bevington P. R., Robinson D. K., 2003, McGraw-Hill, New York

Bhattacharjee P., 2022, arXiv preprint arXiv:2208.14763

Bohr N., 1913, The London, Edinburgh, and Dublin Philosophical Magazine and Journal of Science, 26, 1

Borriello E., Cuoco A., Miele G., 2009, Physical Review D—Particles, Fields, Gravitation, and Cosmology, 79, 023518

Burke B. F., Graham-Smith F., Wilkinson P. N., 2019, An introduction to radio astronomy. Cambridge University Press

Cassidy D. B., Mills Jr A., 2007, Nature, 449, 195

Chaisson E. J., Malkan M. A., 1976, Astrophysical Journal, vol. 210, Nov. 15, 1976, pt. 1, p. 108-112., 210, 108

Condon J. J., Ransom S. M., 2016, Essential radio astronomy. Vol. 2, Princeton University Press

Deutsch M., 1951, Physical Review, 82, 455

Eppel F., et al., 2024, Astronomy & Astrophysics, 684, A11

Fossati G. a., Maraschi L., Celotti A., Comastri A., Ghisellini G., 1998, Monthly Notices of the Royal Astronomical Society, 299, 433

Ghosh P., 2024, Antimatter: Scientists freeze positronium atoms with lasers

Jung D.-W., Lee K. Y., Yu C., 2022, Physical Review D, 105, 095023

Kellermann K., et al., 1989, The Astrophysical Journal, 98

Komatsu E., et al., 2009, The Astrophysical Journal Supplement Series, 180, 330

Kraus A., 2007

Leisi H. J., 2006, Quantenphysik, Eine Einführung anhand elementarer Experimente. Springer

Liu L., Chronopoulos C., 2008, Massachusetts Institute of Technology

Mannheim K., Siegert T., 2024, Lecture: Introduction to Astrophysics, University of Würzburg

Morello V., Rajwade K., Stappers B., 2022, Monthly Notices of the Royal Astronomical Society, 510, 1393

NASA S. M. D., 2010, Introduction to the Electromagnetic Spectrum, https://science.nasa.gov/ems/01_intro

Nguyen H., et al., 2021, Astronomy & Astrophysics, 651, A88

Perley R. A., Butler B. J., 2017, The Astrophysical Journal Supplement Series, 230, 7

Rees W. G., 2001, Interaction of electromagnetic radiation with the Earth's atmosphere. Cambridge University Press

Rohlfs K., Wilson T. L., 2013, Tools of radio astronomy. Springer Science & Business Media

Rosswog S., Brüggen M., 2007, Introduction to High-Energy Astrophysics. Cambridge University Press

Rybicki G., Lightman A., 1979, Radiative processes in astrophysics. Wiley-VCH, Weinheim

Scholz M., 2018, Die Physik der Sterne. Springer Spektrum, Berlin, Heidelberg

Siegert T., 2023, Astrophysics and Space Science, 368, 27

Siegert T., et al., 2016, Astronomy & Astrophysics, 586, A84

Staveley-Smith L., Bond E., Bekki K., Westmeier T., 2022, Publications of the Astronomical Society of Australia, 39, e026

Storm E., Jeltema T. E., Splettstoesser M., Profumo S., 2017, The Astrophysical Journal, 839, 33

Thorne J., Robotham A., Davies L., Bellstedt S., 2022, Zenodo. doi, 10, 5281

Urry C. M., Padovani P., 1995, Publications of the Astronomical Society of the Pacific, 107, 803

Winkel B., Kraus A., Bach U., 2012, Astronomy & Astrophysics, 540, A140

Zijlstra A. A., Van Hoof P., Perley R., 2008, The Astrophysical Journal, 681, 1296

Appendix

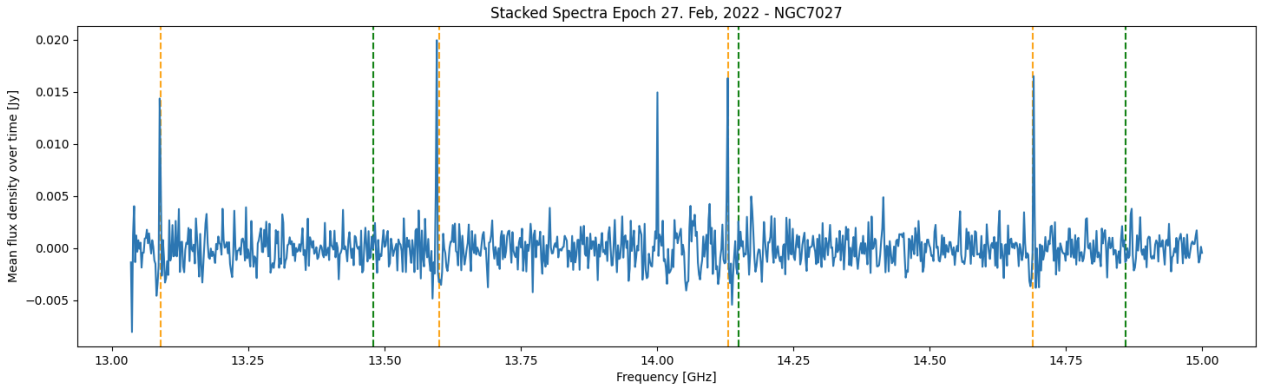

Figure A.1: Stacked calibrated spectra of NGC7027 for the Epoch of the 27. Feb, 2022 are shown. The over time integrated Flux Density is shown versus the Frequency. RFI below 13.1 GHz is removed, RFI at 14 GHz is visible. The calculated frequencies of recombination lines of hydrogen are marked in orange. Similar, the lines for positronium are marked as green dotted lines.

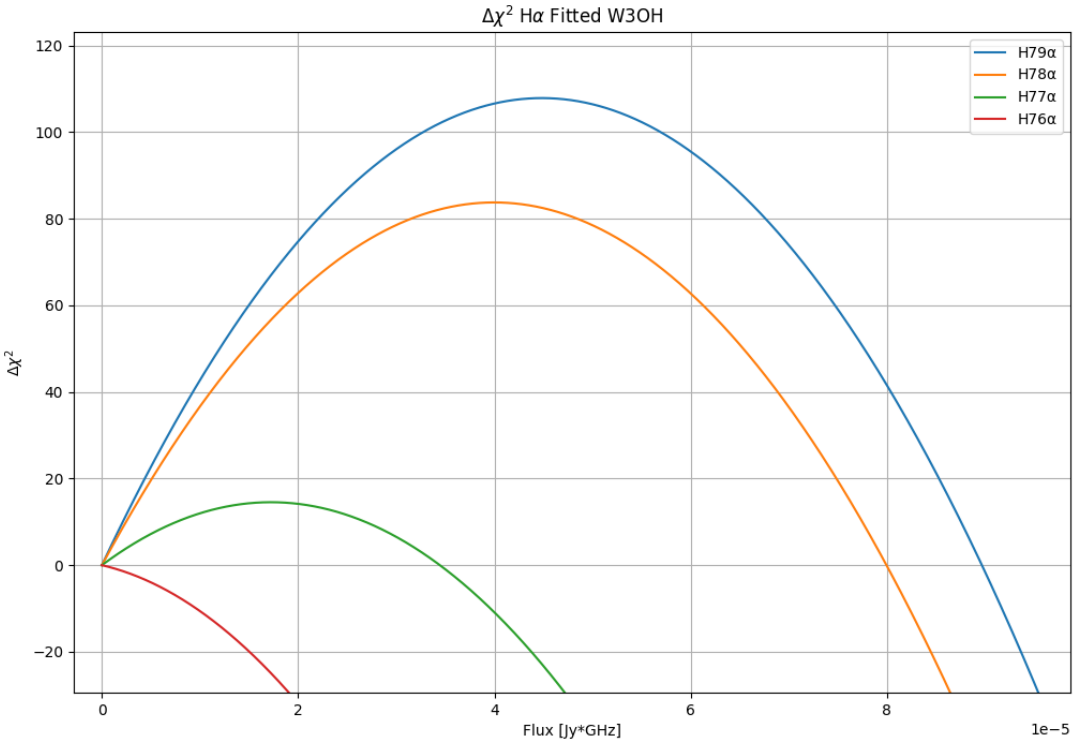

Figure A.2: $\Delta\chi^2(F)$ plotted over the flux for all three expected hydrogen recombination lines within the frequency range of 13–15 GHz. The maxima of the curves represent the significance of the lines. For H79α=10.4σ, for H78α=9.2σ and for H77α=3.8σ. For H76α the Gaussian fit did not converge successfully due to large disturbances around the frequency of the expected line.

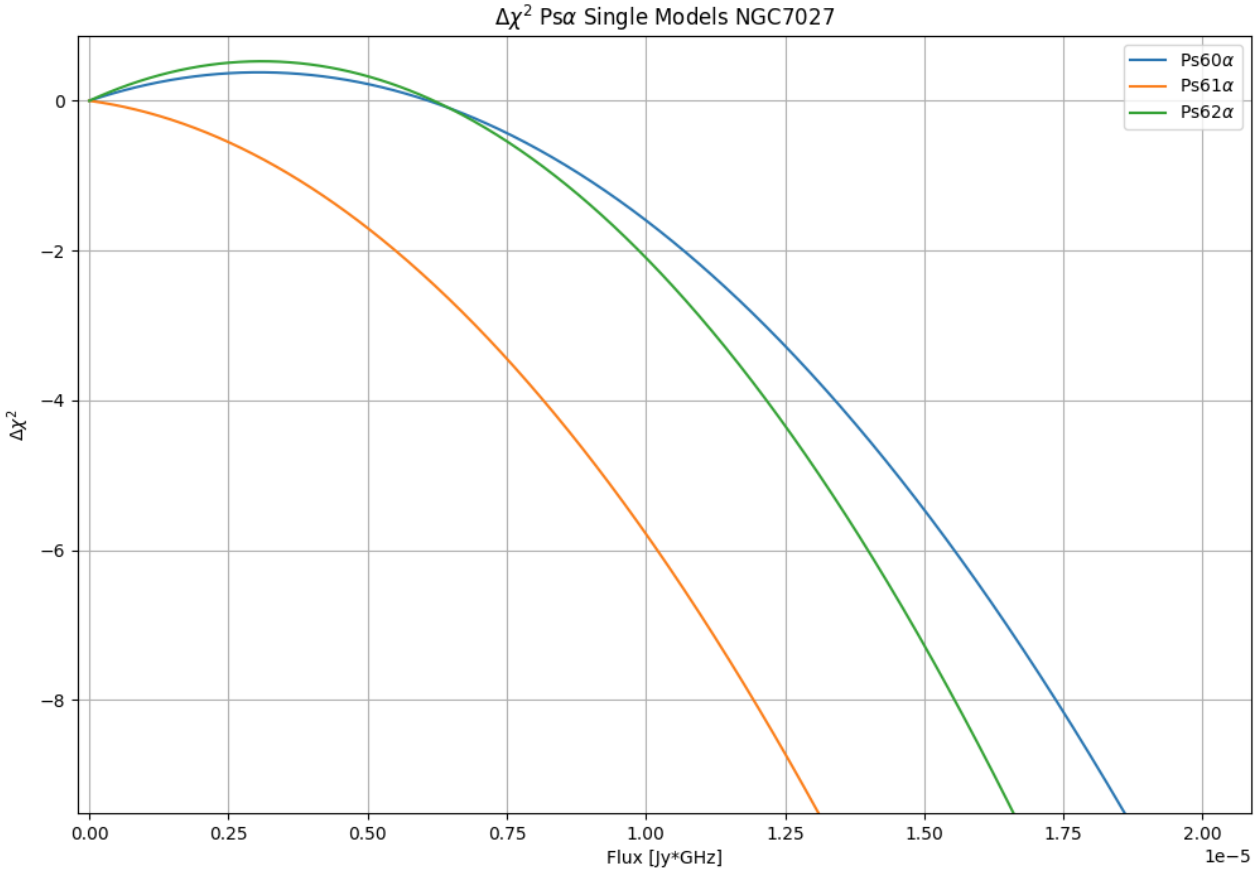

Figure A.3: $\Delta\chi^2(F)$ plotted over the flux for all three expected positronium recombination lines within the frequency range of 13-15 GHz calculated with the "single" method for all scans of NGC7027. Comparing the two models χ_0^2 (linear approximation) and χ_1^2 (linear approximation with Gaussian added). The maxima of the curves represent the significance of the expected $Ps\alpha$ lines.

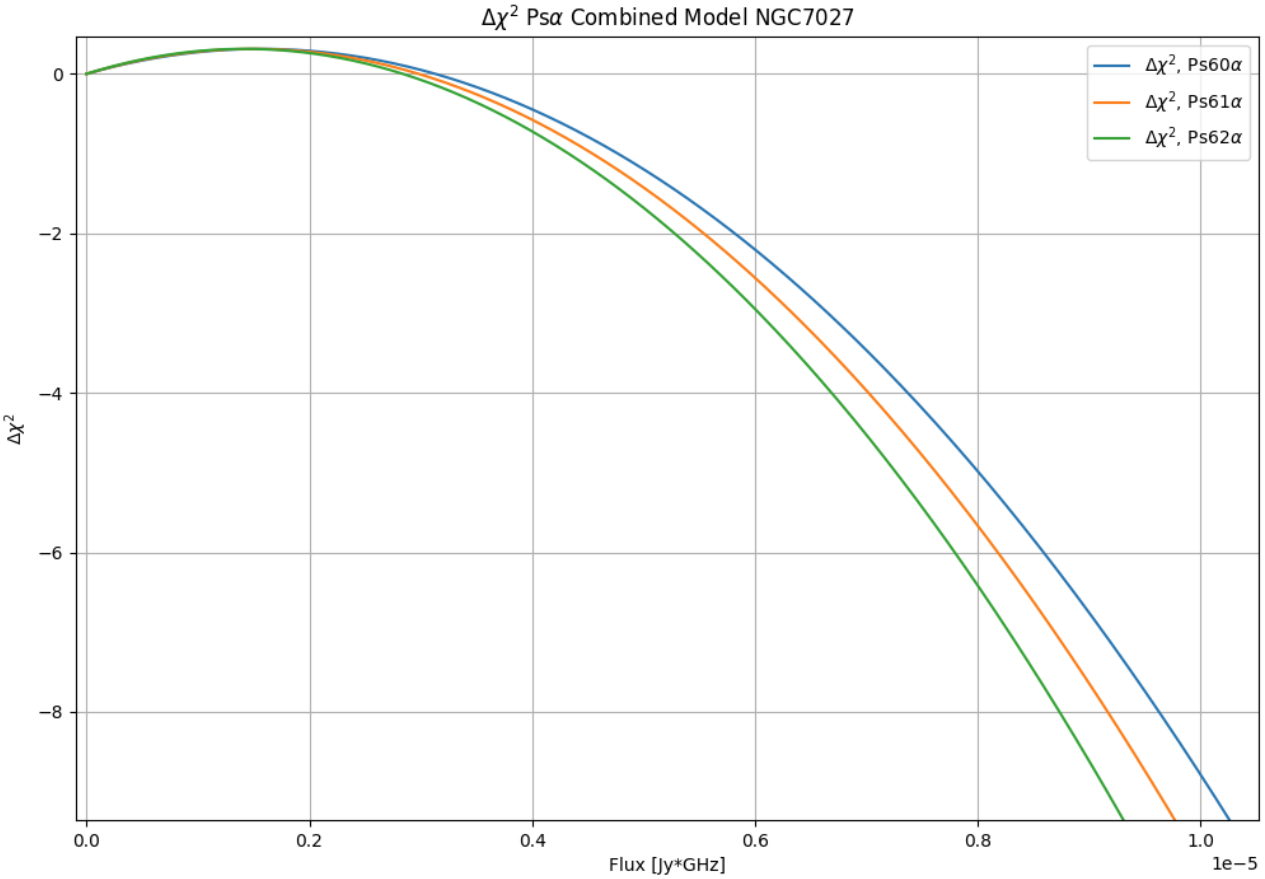

Figure A.4: $\Delta\chi^2(F)$ plotted over the flux for all three expected positronium recombination lines within the frequency range of 13-15 GHz calculated with the "combined" method for all scans of NGC7027. Comparing the two models χ_0^2 (linear approximation) and χ_1^2 (linear approximation with Gaussian added). The maxima of the curves represent the significance of the expected $Ps\alpha$ lines.

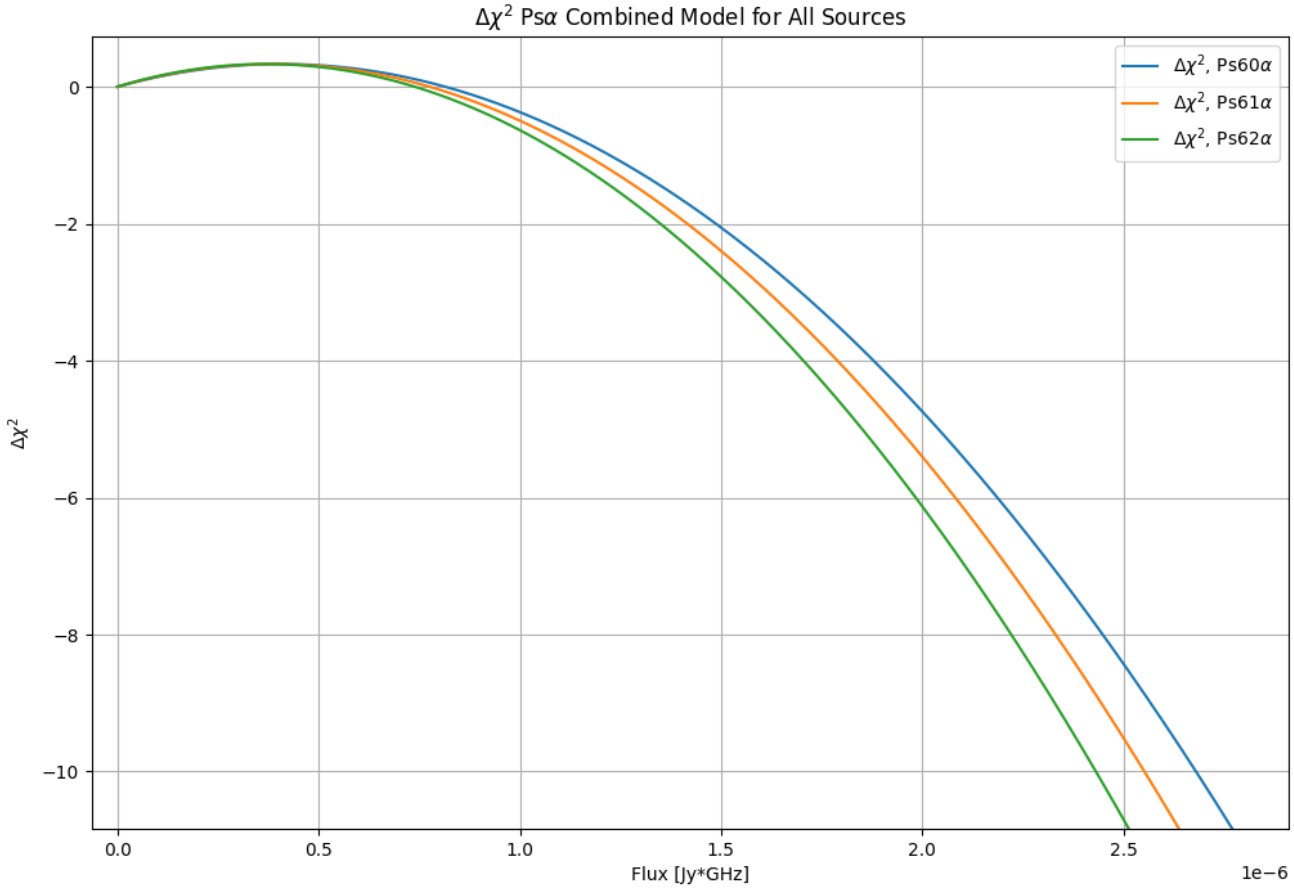

Figure A.5: $\Delta\chi^2(F)$ plotted over the flux for all three expected positronium recombination lines within the frequency range of 13-15 GHz calculated with the "combined" method for all 1715 target scans overlaid. Comparing the two models χ_0^2 (linear approximation) and χ_1^2 (linear approximation with Gaussian added). The maxima of the curves represent the significance of the expected $Ps\alpha$ lines.

Acknowledgments

I would like to express my gratitude to Prof. Matthias Kadler for his guidance and support throughout this thesis, as well as to my supervisors, MSc. Jonas Heßdörfer, MSc. Florian Eppel, and Dr. Thomas Siegert, for their invaluable advice, constructive feedback at every stage of the work, the proofreading of my thesis, and for warmly welcoming me into the Chair of Astronomy at the University of Würzburg. I am also thankful to Prof. Ingo Scholtes from the CAIDAS-Chair of Computer Science for serving as the second evaluator for my thesis.

My thanks go to Dr. Uwe Bach from the Max Planck Institute for Radio Astronomy in Bonn for his assistance regarding observations with the Effelsberg 100 m radio telescope.

I am also grateful to my family and my partner Paula for their support, whether through reviewing this work or providing encouragement throughout the process. Lastly, I would like to thank my colleagues, particularly Felix, for insightful discussions and their readiness to help with any questions.

Based on observations with the 100 m telescope of the MPIfR (Max-Planck-Institut für Radioastronomie) in Effelsberg within the TELAMON project.

Declaration of authorship

I, Lovis Haury, declare that this thesis titled, 'Search for Positronium Recombination Lines with the Effelsberg 100m Radio Telescope' and the work presented in it are my own. I confirm that:

- This work was done wholly or mainly while in candidature for a research degree at this University.
- Where any part of this thesis has previously been submitted for a degree or any other qualification at this University or any other institution, this has been clearly stated.
- Where I have consulted the published work of others, this is always clearly attributed.
- Where I have quoted from the work of others, the source is always given. With the exception of such quotations, this thesis is entirely my own work.
- I have acknowledged all main sources of help.

Signed: _____

Date: _____